Receiver function study in northern Sumatra and the Malaysian peninsula

Katrin Kieling, Dirk Roessler, Frank Krueger

Journal of Seismology manuscript No.
(will be inserted by the editor)

Receiver function study in northern Sumatra and the Malaysian peninsula

Katrin Kieling · Dirk Roessler · Frank Krueger

Received: date / Accepted: date

Abstract In this receiver function study we investigate the structure of the crust beneath six seismic broadband stations close to the Sunda Arc formed by subduction of the Indo-Australian under the Sunda plate. We apply three different methods to analyse receiver functions at single stations. A recently developed algorithm determines absolute shear wave velocities from observed frequency dependent apparent incidence angles of P-waves. Using waveform inversion of receiver functions and a modified Zhu and Kanamori algorithm, properties of discontinuities such as depth, velocity contrast, and sharpness are determined. The combination of the methods leads to robust results. The approach is validated by synthetic tests.

Stations located on Malaysia show high shear wave velocities (V_S) near the surface in the range of 3.4 to 3.6 kms^{-1} attributed to crystalline rocks and 3.6 to 4.0 kms^{-1} in the lower crust. Upper and lower crust are clearly separated, the Moho is found at normal depths of $30 - 34$ km where it forms a sharp discontinuity at station KUM or a gradient at stations IPM and KOM. For stations close to the subduction zone (BSI, GSI, PSI) complexity within the crust is high. Near the surface low V_S of $2.6 - 2.9\,\mathrm{kms}^{-1}$ indicate sediment layers. High V_S of $4.2\,\mathrm{kms}^{-1}$ are found at depth greater than 6 km and 2 km at BSI and PSI, respectively. There, the Moho is located at 37 and 40 km depth. At station GSI, situated closest to the trench, the subducting slab is imaged as a north-east dipping structure separated from the sediment layer by a 10 km wide gradient in V_S between 10 and 20 km depth. Within the subducting slab $V_S \approx 4.7$ km. At station BSI the subducting slab is found at depth between 90 and 110 km dipping $20° \pm 8°$ in approximately N60°E. A velocity increase in similar depth is indicated at station PSI, however no evidence for a dipping layer is found.

Keywords receiver functions · absolute shear wave velocity · Sumatra · subduction zone structure

PACS 91.30.Wx

Katrin Kieling
Institute of Geosciences, University of Potsdam, now at GFZ German Research Centre for Geosciences, Telegrafenberg, D-14473 Potsdam, Germany
Tel.: +49-331-2881288
E-mail: katrin.kieling@gfz-potsdam.de

Dirk Rößler E-mail: d-roessler@web.de · Frank Krüger E-mail: kruegerf@geo.uni-potsdam.de
Institute of Geosciences, University of Potsdam, K.-Liebknecht-Str. 24/25, 14471 Golm,Potsdam, Germany

1 Introduction

The Sunda (volcanic) Arc (Fig. 1) is caused by subduction of the oceanic Indo-Australian plate underneath the Sunda plate, which started during the Cretaceous i. e. $\sim$ 100 Ma ago (Hamilton, 1979). It extends about 6000 km from the Andaman Islands in the north-west to the Lesser Sunda Islands in the south-east. The region is a formidable natural geologic laboratories and permits to study the behaviour of the lithosphere in subduction zones, not least due to such extreme events as the tsunamigenic 2004 earthquake or the Toba eruption $\sim$ 74,000 years ago.

Along Sumatra Baroux et al (1998) found a convergence with obliquity of 20° up to 30°. Subarya et al (2006) report a convergence rate of 65 mm/yr. The Regional Upper Mantle (RUM) model by Gudmundsson and Sambridge (1998) infers the geometry of the slab from seismicity (see Fig. 1 for the western part of Sumatra). It shows that the depth of the slab varies from

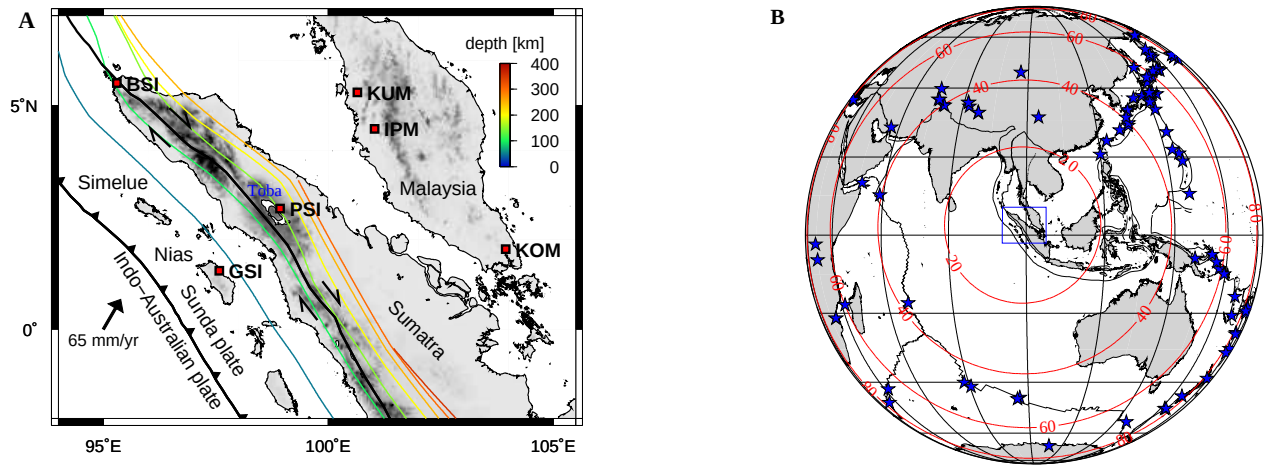

Fig. 1 **A** Map of Sumatra with considered stations (squares, compare Tab. 1) and major faults. Colours of isolines indicate depth of the subducted slab (Gudmundsson and Sambridge, 1998). **B** Earthquakes (stars) used for receiver function analysis. Red lines show epicentral distance from station PSI in degree. The central blue rectangle outlines the region shown in A.

600 km in eastern Java to 300 km in northern Sumatra. From tomographic studies of this and other subduction zones and modelling (Widiyantoro and van der Hilst, 1996; Gorbatov et al, 1999) it is known that the subducting plate forms a cold, high-density slab with P- and S-wave velocities 5-10% higher than in the surrounding normal mantle. However, only little is known regarding the crustal and upper mantle shear wave velocity structure of the whole region from global surface wave studies with rather limited resolution (e.g. Ritzwoller et al, 2002). In recent years extensive reflection seismic studies of the region were carried out, e. g. by Kopp et al (2001); Singh et al (2008); Franke et al (2008) mapping the uppermost 10-20 km of the crust offshore Sumatra. Furthermore Wu et al (2005) studied the regional S-velocity of the South China Sea and provides S-velocity maps in several depths.

The subduction has significant impact on the upper mantle and the crust of the overriding plate. Increasing pressure at depth causes slab dehydration (Rüpke et al, 2004) and the transition from gabbro to eclogite. Fluids are released in the lithosphere. They cause serpentinisation and reduce the melting temperatures of peridotite rocks (Gill, 1981; Hacker et al, 2003). This leads to the generation of low-density magma which rises and intrudes or extrudes on the upper lithosphere, forming a chain of volcanoes. The significance of the volcanic activity is demonstrated for example by the Toba caldera (see Fig. 1). It is an $\approx 30 \times 100$ km large topographic depression in northern Sumatra which was formed during several eruptions over the last 1.2 million years. Geologic maps (e. g. Crow and Barber, 2005) show large areas dominated by intrusive rocks such as granite or gabbro as well as extrusive rocks such as andesite or basalt. While those are often covered by a sedimentary unit on Sumatra, the volcanic rocks are directly exposed on the surface at the Malaysian peninsula.

The Malaysian peninsular is characterised by the Betong-Raub suture zone (Metcalfe, 2000), which was formed during the subduction of the Paleo-Thethys Ocean beneath Indochina during the Late Paleozoic and the collision of the Sibumasu Terrane with Indochina.

Receiver functions are widely employed to detect P-to-S-converted waves and are especially useful to image seismic discontinuities if dense networks of high-quality three-component broadband stations are installed. However, in many regions of the Earth the only available information regarding the shear wave velocity depth profile is due to relatively isolated stations. Classical receiver function methods for single stations include picking of difference traveltimes for direct conversions and multiples and estimation of the corresponding discontinuity depth with an average background model (e.g. Krueger et al, 2002); estimation of discontinuity depth and V_P/V_S ratio by stacking direct Ps conversion and multiple waveforms in a gridsearch procedure (Zhu and Kanamori, 2000); inversion of stacked receiver functions for 1D shear wave models (Ammon, 1991). The retrieval of absolute shear wave velocities from receiver functions is still a major challenge. Several studies applied combined inversions of receiver functions and phase-/group-velocity dispersion curves from surface waves to stabilise the inversion (e.g. Julià et al, 1998; Chang et al, 2004). Recently Svenningsen and Jacobsen (2007) proposed to use the frequency dependent apparent incidence angle of receiver functions to estimate absolute shear wave velocities as well as depths of discontinuities. The latter method has the advantage that local velocity models can be retrieved.

The aim of this study is twofold. First, crustal seismic properties in the study region are investigated exploiting different single station receiver function techniques. We use the method of Svenningsen and Jacobsen (2007) to retrieve initial absolute shear wave velocity models by a gridsearch technique. In a next step this velocity model is used to invert for 1D models (see e. g. Kind et al, 1995, Jacobsen and Svenningsen, 2008) using receiver function waveforms and fixed V_P/V_S ratios. We find the V_P/V_S ratio of the top layer and the depths of discontinuities following the approach of Zhu and Kanamori (2000) but fixing V_S instead of V_P, what enables us to link the analysis of apparent incidence angles directly to the technique of Zhu and Kanamori. This modified algorithm is referred to as MZK from hereon. Since all methods give the depth of discontinuities the consistency of the results can be checked. Furthermore we test the effect of velocity gradients on the outcome of the different methods.

In a second step, based on the analysis of the crustal properties, structures related to the subduction zone in the upper mantle are investigated. With the help of lateral and azimuthal variations of conversion depths found from receiver functions, the dip of the subducting plate is constrained beneath two stations.

2 Methodology

The receiver function method takes advantage of the fact that a seismic compressional wave (P-wave) impinging obliquely on a discontinuity is partly refracted as a P-wave and partly converted to a shear wave (S-wave) (see Fig. 2). Besides the direct P-to-S converted Ps-wave there are also the multiple reverberations PpPs and PpSs (see Fig. 2) that have a comparable amplitude to the Ps phase. Delay times and amplitudes of direct and multiple phases provide information about the depth of a discontinuity and the impedance contrast. For a 1D structure traveltime differences depend on wave type and slowness only.

The calculation of receiver functions mainly involves two steps. First, seismograms are rotated to the LQT-coordinate system of the ray assuming theoretical back-azimuths and incidence angles (Kind et al, 1995). We used incidence angles given by Hoang-Trong and Behe (1972). By this rotation the P-wave signal should be minimised on the Q-component. This improves visibility of shallow layers. However, artificial phases appear on Q-components when incorrect angles are used for rotation. The true azimuth deviates from the theoretical value by less than 10°. Deviations in incidence angles are larger. Most likely, these deviations in incidence angle are due to erroneous assumptions on velocities of

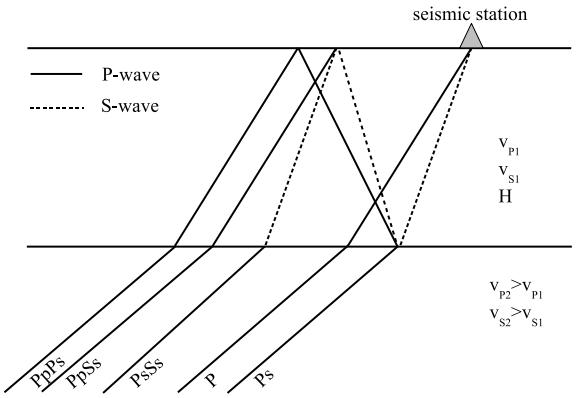

Fig. 2 Ray diagram of phases used for receiver function analysis in a two-layer model. The incident P-wave converts at depth H into the refracted P- and S-waves and their multiples within the horizontal layer.

shallow layers but not caused by distant deep structures. As we want to take these shallow layers into account during waveform inversion, we also want to consider the phases at zero time. After rotation, a deconvolution in the time domain is performed by Wiener filtering (Kind et al, 1995). The deconvolution is stabilised by adding a constant 0.1 to the diagonal elements of the filter matrix. This corresponds to intermediate stabilisation (Svenningsen, 2007). The calculation of the inverse filter depends on the length of the source-time function and the arrival time of later phases. In this study we chose window lengths between 80 and 140 s following the direct P-wave. This inverse filter is applied to the Q- and T-components to obtain Q- and T-receiver functions.

2.1 Investigation of apparent incidence angles

The apparent incidence angle of the incoming P-wave results from the superposition of the incoming and the reflected wavefield. It can be used to estimate absolute S-wave velocities from receiver functions (Svenningsen and Jacobsen, 2007) based on the relation

$$\frac{\sin\left(\frac{\bar{i}_P}{2}\right)}{V_S} = \frac{\sin(i_P)}{V_P} = p \qquad (1)$$

given by Wiechert (1907). Here, p, i_P, and $\bar{i}_P$ are the slowness, the theoretical incidence angle, and the apparent incidence angle of the direct P-wave, respectively. The latter can be measured. Hence, calculating the slowness with the help of IASP91 reference model (Kennett, 1991) and measuring $\bar{i}_P$, V_S underneath a station can be retrieved. Typically the apparent angle of incidence is determined by dividing the R- by the Z-component of the receiver function (Svenningsen

and Jacobsen, 2007). In this study, we use the Q- and L-component and add the theoretical incidence angle which was used for rotation (see formula 2). Receiver functions are convolved with a squared cosine of width T, resulting in low-pass filtering. The convolution is evaluated at time zero which results in an apparent incidence angle dependent on the low-pass parameter T,

$$\bar{i}_{\mathrm{P}}(T) = \arctan\left[\frac{\int_{(-T)}^{T} \mathrm{rf_Q}(\tau)\cos^2(\frac{\pi\tau}{2T})d\tau}{\int_{(-T)}^{T} \mathrm{rf_L}(\tau)\cos^2(\frac{\pi\tau}{2T})d\tau}\right] + i_{\mathrm{ROT}}, \quad (2)$$

where $\mathrm{rf_Q}$ and $\mathrm{rf_L}$ are Q- and L-components of the receiver function and i_{ROT} is the incidence angle which was used for rotation to the LQT-system. Inserting (2) into (1) gives a T-dependent V_{S} denoted as apparent velocity $V_{\mathrm{S,app}}$

$$V_{\mathrm{S,app}}(T) = \frac{\sin\left[\frac{\bar{i}_{\mathrm{P}}(T)}{2}\right]}{p}. \quad (3)$$

With increasing T the calculation window increases and direct conversions and their multiples affect $\bar{i}_{\mathrm{P}}(T)$. Thus, for higher values of T, the apparent velocity can be associated to a higher depth (see Fig. 3B,C). For a detailed description of the method see Svenningsen and Jacobsen (2007). For a model consisting of a layer over a halfspace the S-wave velocities can be directly read from the $V_{\mathrm{S,app}}(T)$ curve. More complicated models require an inversion of the $V_{\mathrm{S,app}}(T)$ curve.

Curves of $V_{\mathrm{S,app}}(T)$ are similar for different slownesses (Svenningsen and Jacobsen, 2007). In the presence of noise, mean curves, $\bar{V}_{\mathrm{S,app}}(T)$, can therefore be formed by stacking $V_{\mathrm{S,app}}(T)$ curves for all receiver functions at one station. They are modelled by the $V_{\mathrm{S,app}}(T)$ curve for a mean slowness which is $6.4\,\mathrm{s}/^{\circ}$ in this study. Models for V_{S} can be retrieved in a grid search by forward modelling of $V_{\mathrm{S,app}}(T)$ from synthetic receiver functions calculated by the Thomson-Haskell method (Kosarev et al, 1987). The best fitting curve was determined by minimising the misfit e_{sd}

$$e_{\mathrm{sd}} = \sum_{T=0.5}^{T=T_{\max}} \sqrt{\left(\bar{V}_{\mathrm{S,app}}(T) - V^{\mathrm{syn}}_{\mathrm{S,app}}(T)\right)^2}, \quad (4)$$

where $V^{\mathrm{syn}}_{\mathrm{S,app}}$ is modelled from synthetic receiver functions. In our study $T_{\max}$ is the largest T for which $\bar{V}_{\mathrm{S,app}}(T)$ is below $5\,\mathrm{kms}^{-1}$. This limit was chosen, as $V_{\mathrm{S,app}}(T)$ tends to diverge for higher values of T, and $5\,\mathrm{kms}^{-1}$ is a reasonable upper limit for V_{S} of the upper mantle. To obtain receiver functions, the theoretical seismograms are treated in the same way as the data.

2.2 Waveform inversion

Receiver functions can also be inverted for V_{S}-depth models by linear inversion. This is non-unique (Ammon et al, 1990) and depends on the starting model. In this study we use the method by Kind et al (1995) and a large number of thin layers which allows quasi-gradient models. Jacobsen and Svenningsen (2008) show that fine layering and a high number of iterations result in more unique results.

2.3 Modified Zhu&Kanamori algorithm (MZK)

A widely used method to extract the depth of discontinuities, H, and the $V_{\mathrm{P}}/V_{\mathrm{S}}$ ratio from receiver functions was introduced by Zhu and Kanamori (2000). This involves stacking of receiver functions within time windows according to predicted delay times of Ps, PpPs, and PpSs and analysis of the stack amplitudes. We use semblance analysis (Neidell and Taner, 1971) to improve resolution. The semblance S within a time window is the energy of the stacked trace divided by the sum of the energies of all traces that make up the stack,

$$S = \frac{\sum_{\tau}\left|\sum_{i=1}^{n} \mathrm{rf}_i(t_{\mathrm{Ps}}) + \mathrm{rf}_i(t_{\mathrm{PpPs}}) + \mathrm{rf}_i(t_{\mathrm{PpSs}})\right|^2}{n\sum_{\tau}\sum_{i=1}^{n}(\left|\mathrm{rf}_i(t_{\mathrm{Ps}})\right|^2 + \left|\mathrm{rf}_i(t_{\mathrm{PpPs}})\right|^2 + \left|\mathrm{rf}_i(t_{\mathrm{PpSs}})\right|^2)} \quad (5)$$

where n equals the number of traces used, rf_i is the receiver function i and t_{Ps}, t_{PpPs} and t_{PpSs} are the delay-times of the conversion and its multiples. τ is the time window of 2 s length arranged symmetrically around the considered times. Delay times and semblances are usually computed in a grid search over H and $V_{\mathrm{P}}/V_{\mathrm{S}}$ by fixing V_{P}. Where semblance is at a maximum the correct H and $V_{\mathrm{P}}/V_{\mathrm{S}}$ ratio are assumed to be found.

Here, we make two modifications. The resulting algorithm is referred to as MZK. First, we assume that V_{S} is given instead of V_{P}, which permits the usage of V_{S}-values as obtained from the analysis of apparent incidence angle and the waveform inversion. Formulas used for calculating delay times are:

$$\begin{aligned} t_{\mathrm{Ps}} &= H\left(\sqrt{V_{\mathrm{S}}^{-2} - p^2} - \sqrt{\left(\tfrac{V_{\mathrm{P}}}{V_{\mathrm{S}}}V_{\mathrm{S}}\right)^{-2} - p^2}\right) \\ t_{\mathrm{PpPs}} &= H\left(\sqrt{V_{\mathrm{S}}^{-2} - p^2} + \sqrt{\left(\tfrac{V_{\mathrm{P}}}{V_{\mathrm{S}}}V_{\mathrm{S}}\right)^{-2} - p^2}\right) \\ t_{\mathrm{PpSs}} &= 2H\sqrt{V_{\mathrm{S}}^{-2} - p^2}. \end{aligned} \quad (6)$$

Reformulation of Eqs. (6) gives the general form $H = H(t, \frac{V_{\mathrm{P}}}{V_{\mathrm{S}}})$. For Ps the slope of the $H(t_{\mathrm{Ps}}, \frac{V_{\mathrm{P}}}{V_{\mathrm{S}}})$ is positive, while for the first multiple the slope of $H(t_{\mathrm{PpPs}}, \frac{V_{\mathrm{P}}}{V_{\mathrm{S}}})$

is negative and for the second multiple $H(t_{\mathrm{PpSs}}, \frac{V_\mathrm{P}}{V_\mathrm{S}})$ is constant (see e.g. Fig. 3G). This results in a more distinct semblance maximum in the $V_\mathrm{P}/V_\mathrm{S}$-$H$-plot and higher resolution of $V_\mathrm{P}/V_\mathrm{S}$. Second, we replace the original layer-over-halfspace model by a two-layers-over-halfspace model. In our study this turns out to be more appropriate because we can often constrain the upper layer from the incidence angle analyses and waveform inversion. Formulas for calculating delay times are given in the appendix. In this study time windows of 2 s length centred around the predicted times t_{Ps}, t_{PpPs}, and t_{PpSs} are used for stacking. All three phases are equally weighted during the stacking.

3 Synthetic Examples

First we study the different effects on receiver functions that can be expected due to sharp seismic discontinuities compared to velocity gradients (Figs. 3C, 4C). For this purpose synthetic seismograms are computed for two simple layer-over-halfspace models. We chose for the upper layer $V_\mathrm{S} = 3.2\,\mathrm{kms}^{-1}$ and $V_\mathrm{P}/V_\mathrm{S} = 1.73$ over a halfspace with $V_\mathrm{S} = 4.6\,\mathrm{kms}^{-1}$, $V_\mathrm{P}/V_\mathrm{S} = 1.79$. The discontinuity and the gradient are located at depths of 29 km and between 25 and 33 km, respectively. Based on these 2 models, receiver functions with a source wavelet of 1 s duration (Küpper, 1958) are calculated and stacked assuming epicentral distances between 27° and 92° (Figs. 3A, 4A). For stacking, receiver functions were moveout corrected assuming Ps, PpPs or PpSs phases and a slowness of 6.4 s/° (Yuan et al, 1997). In the single traces we find that the converted phases are broadened in the gradient model compared to conversion at the sharp discontinuity. The effect is most pronounced for the PpPs and PpSs multiples. In the moveout stacked receiver functions the waveform of the reference phase retains its shape while the other phases are artificially broadened. This effect is most pronounced in the discontinuity model for the multiples when Ps is assumed (Figs. 3A, top traces). Ignoring this distortion, discontinuities may be misinterpreted as gradients. Resulting $V_{\mathrm{S,app}}(T)$ curves are only marginal different for both models (Figs. 3B,C and 4B,C). Therefore, we cannot expect to discriminate between a sharp discontinuity and a gradient from $V_{\mathrm{S,app}}(T)$. It turns out that the short-period part of the $V_{\mathrm{S,app}}(T)$ curve is usually stable and equals V_S of the upper layer.

During waveform inversions mismodelling from stacking was avoided by limiting the considered distance range to $47° - 67°$, what corresponds to a slowness range of $6.4 - 7.8$ s/° and allows to stack a sufficient number of receiver functions at each station. For the inversions synthetic receiver functions were calculated for a slowness of 7.08 s/° (57° epicentral distance), since this is the mean slowness of the stacked receiver functions. We invert receiver functions for V_S-depth models with $V_\mathrm{S}/V_\mathrm{P}$ fixed at 1.73 in the crust and 1.79 in the mantle. Densities in the crust are calculated using Birch's law (Birch, 1961), but fixed to $3.3\,\mathrm{g/cm}^3$ in the mantle. Because of their non-uniqueness, 200 inversions with different starting models are performed. They are randomly selected from a uniform distribution within $\pm 0.75\,\mathrm{km}^{-1}$ around the initial reference model which is obtained from $V_{\mathrm{S,app}}(T)$ analysis (see Figs. 3D-F and 4D-F). The distribution of the results is analysed. Out of those, the model with the best misfit is searched. For the calculation of a mean model only those models with a misfit of maximal 4 times the global best misfit are used. By this we correctly reproduce the position of the discontinuity and of the gradient, the velocities of both layers (see Figs. 3D, 4D), and the waveforms (Figs. 3E,F and 4E,F).

Major differences due to the model differences are found by the MZK (Figs. 3G and 4G). As mentioned before, the slopes $H(t, \frac{V_\mathrm{P}}{V_\mathrm{S}})$ (coloured curves in Figs. 3G and 4G) differ in sign depending on phase type. This leads to a distinct intersection of the three functions at the expected depth and $V_\mathrm{P}/V_\mathrm{S}$ ratio and reduced smearing along the curves (Fig. 3G). For the sharp discontinuity the depth can be found in the grid search at 29 km and $V_\mathrm{P}/V_\mathrm{S} = \sqrt{3}$. Both equal the original model. In the case of the gradient, however, the method is almost insensitive to $V_\mathrm{P}/V_\mathrm{S}$. No single depth of conversion can be found but the broad semblance maximum resembles the location of the gradient. Therefore, fixing shear wave velocities to values obtained in prior inversions we expect to distinguish between sharp seismic contrasts and gradient. The finding of $V_\mathrm{P}/V_\mathrm{S}$ seems promising for first order seismic discontinuities but not in case of velocity gradients.

4 Application to stations along Sunda Arc and Malaysia

4.1 Data and processing

We study crustal and upper mantle seismic structures on northern Sumatra and the Malaysian Peninsula. Receiver functions were calculated at 6 stations that had been in operation for several years (Fig. 1A, Tab. 1). 112 earthquakes within epicentral distances of $30° - 96°$ and magnitudes $\mathrm{m_B} \geq 5.8$ were chosen (Fig. 1B). The resulting backazimuthal event distribution is uneven with a majority in north-east (Japanese and Kuril islands) and south-east (Kermadec-Tonga subduction zone). The number of calculated receiver functions per

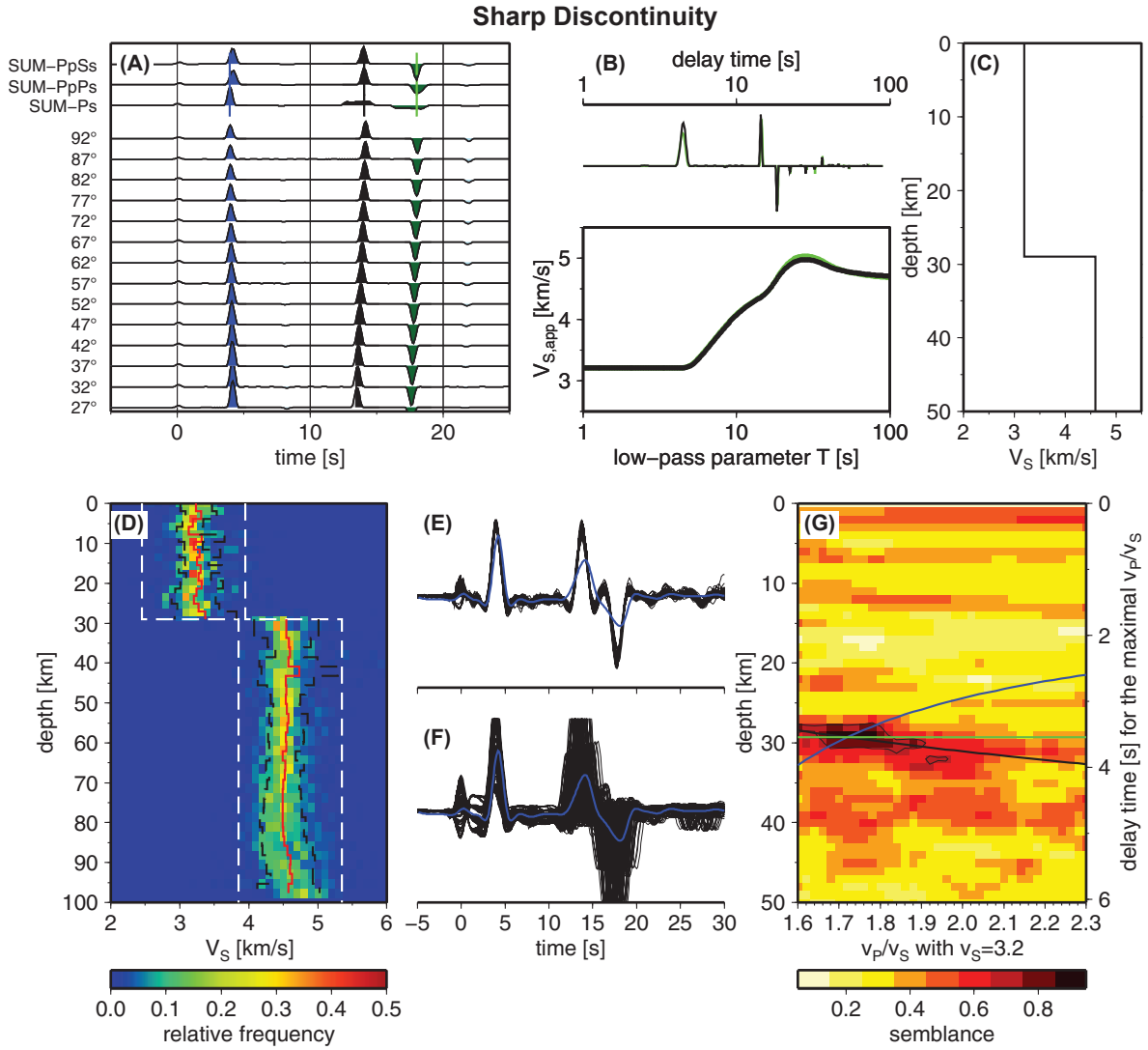

Fig. 3 Analysis of synthetic receiver functions computed for a model consisting of a layer (thickness: 29 km, V_S = 3.2 kms^{-1}, V_P/V_S = 1.73) over a halfspace (V_S = 4.6 kms^{-1}, V_P/V_S = 1.79). **A** Synthetic receiver functions for events in different epicentral distances (annotated on the left). Important phases also discussed in the text are highlighted. Blue, black, and green ticks mark arrival of the primary Ps conversion and associated PpPs and PpSs multiples (compare G). Top three traces: summation with moveout corrections for the Ps, PpPs, and PpSs phases assuming a slowness of 6.4 s/° (67 ° epicentral distance). **B** Synthetic receiver function (6.4 s/° (black), top) and derived $V_{S,app}(T)$ curve (bottom) with logarithmic time axes. For comparison, receiver functions and derived $V_{S,app}(T)$ curve for a slowness of 5.0 s/ are shown in green. **C** V_S-depth model corresponding to the $V_{S,app}(T)$ curve in B. **D** Density function of the V_S-depth models from 200 inversions. For inversion, synthetic receiver functions in A were stacked within 47-67° epicentral distance. White dashed lines: range limit of starting models around the V_S derived from $V_{S,app}(T)$ in B. Red solid and black dashed lines: resulting medium velocities and standard deviations. **E** Receiver functions predicted by the models obtained from 200 inversions in D. Blue line: original receiver function, low-pass filtered at 1 Hz. It results from stacking receiver functions for epicentral distances between 47 ° and 67 ° (without moveout correction). **F** Same as E but for receiver functions corresponding to the starting models. **G** Results of MZK inversions assuming one layer (V_S = 3.2 kms^{-1}) above a halfspace. Thin black line indicates the area with values greater than 75% of the semblance maximum. For comparison with receiver functions in A, delay times (right y-axis) are calculated with V_P/V_S given at semblance maximum. Blue, black, and green lines show conversion depth curves H (Eqs. 6) for given V_P/V_S ratios and travel time differences. The latter correspond to the ticks in A (upper three traces) with the same colour.

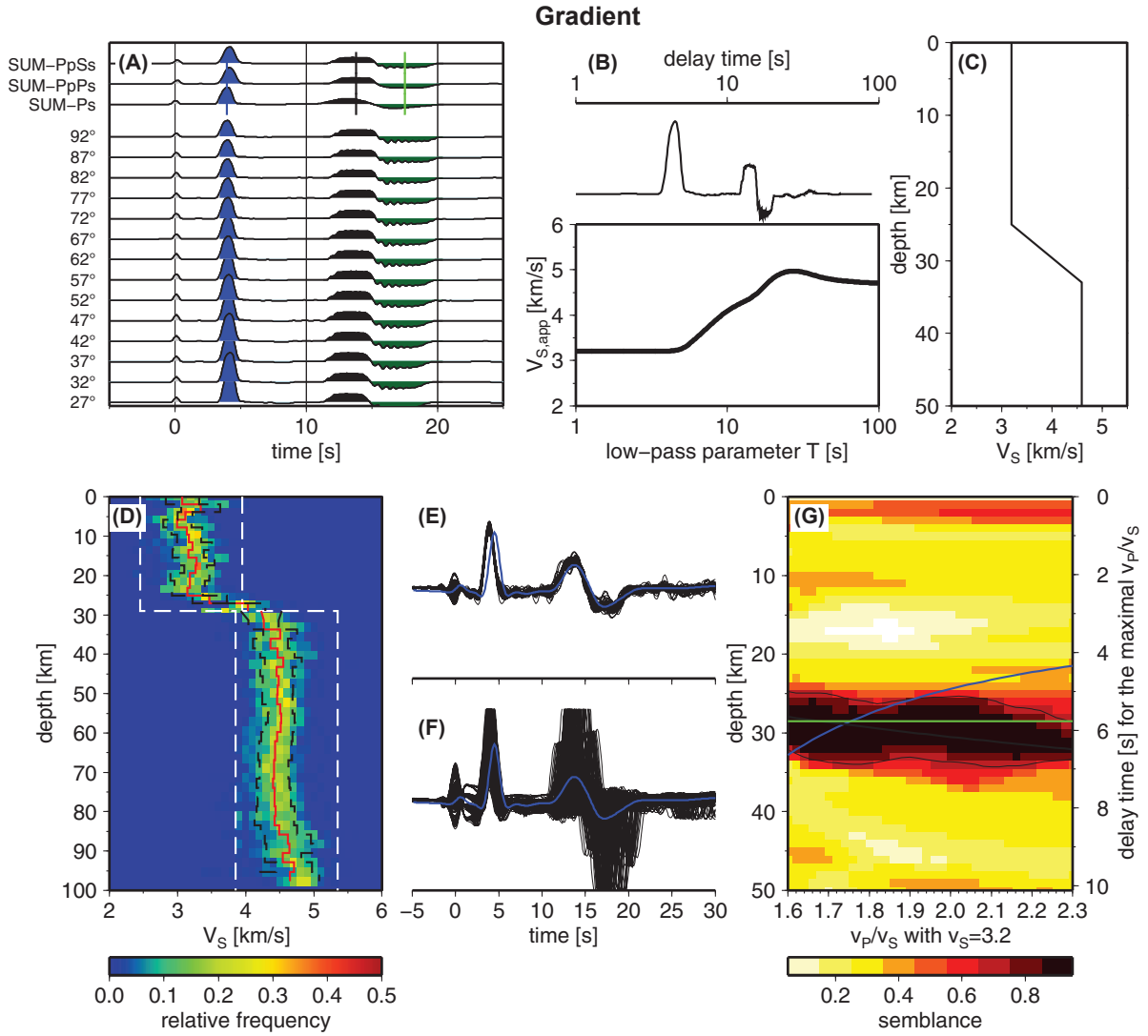

Fig. 4 Same as Fig. 3 but for a synthetic model containing a velocity gradient at 25 to 33 km depth. PpPs and PpSs multiples (A, B, E, F) and the band of high semblance (G) are broadened. Semblance by the MZK (G) becomes almost insensitive to V_P/V_S.

station varies with station operation time and due to different data quality (Tab. 1). Data processing was carried out manually. Erroneous and low-quality data were rejected. Seismograms were processed in the same way as the synthetics in section 3. Table 2 summarises the results for the considered stations and methods.

Long period noise may obscure the $V_{S,app}(T)$ curves (Svenningsen and Jacobsen, 2007). The modelling of $V_{S,app}(T)$ was therefore refined to include only high quality receiver functions. First, only receiver functions with signal-to-noise ratio > 2 before and after low-pass filtering at 0.2 Hz are accepted. $V_{S,app}(T)$ curves are calculated from the remaining receiver functions. The mean and the standard deviation are computed at every point of the curves. An improved mean curve ($\bar{V}_{S,app}(T)$) is found by rejecting again all curves, which exceed the limit of one standard deviation in the range $1\,s \leq T \leq 7\,s$. This selection of high-quality receiver functions finally leads to stable mean curves. They are used to find a V_S-depth model in a grid search. Stability is tested by jack-knifing i.e. the grid search was repeated 160 times including only 60% of all available $V_{S,app}(T)$ curves that were randomly selected to form $\bar{V}_{S,app}(T)$. For stations BSI and PSI observed $\bar{V}_{S,app}(T)$ curves cannot be explained by three-layer models. Therefore, a fourth layer was added. The velocity of the uppermost layer was always read directly from $\bar{V}_{S,app}(T)$ within the interval $0.2\,s < T < 0.5\,s$. The velocities of the following layers where allowed to vary between $3.0\,kms^{-1} < V_S < 5.6\,kms^{-1}$ in steps of $0.2\,kms^{-1}$. Depths were searched from 0 to 60 km in steps of 1 km. Density plots show the relative frequency of the obtained models as well as the median model and the standard deviation (e. g. Fig. 5c). Waveform inversion

station	RF	RF(47-67°)	network	seismometer	latitude [°N]	longitude [°E]	starting date
BSI	64	29	JISNET	CMG-3T/100	5.49	95.29	01-Jan-2000
GSI	65	23	GEOFON	STS-2	1.30	97.57	02-Oct-2005
IPM	65	22	MY	STS-2	4.48	101.03	29-Mar-2006
KOM	61	18	MY	STS-2	1.79	103.84	29-Mar-2006
KUM	83	25	MY	STS-2	5.29	100.65	17-Feb-2005
PSI	75	31	PS	STS-2	2.69	98.92	29-Mar-1993

Table 1 Station specifications and total number of calculated receiver functions (RF) and for earthquakes within 47-67° epicentral distance (compare Fig. 1). Networks are: MY – Malaysian National Seismic Network, PS – Pacific21, GEOFON – GeoForschungsZentrum Potsdam, and JISNET – Japan-Indonesia Seismic Network.

is limited to receiver functions within a slowness range of $6.4 - 7.8\,\mathrm{s}/^\circ$. Initial models are based on the outcome of the $V_{\mathrm{S,app}}(T)$ modelling. A mean model is calculated based on the models with misfits smaller than four times the best misfit in case of Malaysian stations and twice the best misfit in case of Sumatran stations. Observed $\bar{V}_{\mathrm{S,app}}(T)$ curves are compared with $V_{\mathrm{S,app}}(T)$ predicted from the outcome of the waveform inversions (red lines in Figs. 5B-10B). Finally, the MZK is applied by fixing V_{S} which was retrieved before. The thickness of the uppermost layer H_1 is constrained by the preceding waveform inversions.

4.2 KUM

Receiver functions at station KUM (Fig. 5A) show positive signals at zero time as well as conversions from a shallow interface at approximately 1 s. The deviations of the observed from the theoretical incidence angle leading to phases at zero time are mainly due to shallow layers near the surface. The Moho conversion at 4 s appears relatively weak. However, corresponding PpPs and PpSs multiples are clear at 13.5 s and 17.5 s. Modelling of $V_{\mathrm{S,app}}(T)$ (Fig. 5B,C) results in a shallow, 3 km thick layer with $V_{\mathrm{S}} = 3.3\,\mathrm{kms}^{-1}$ followed by increased velocities of $V_{\mathrm{S}} = 3.6\,\mathrm{kms}^{-1}$ down to a depth of 25 km. Velocities are well defined by this method. Depth resolution turns out to be weaker and the variability of the lower depth limit is high.

By waveform inversion the uppermost layer is unresolved (Fig. 5D) but a discontinuity at approximately 19 km is indicated. For this upper layer $V_{\mathrm{S}} = 3.5\,\mathrm{kms}^{-1}$. Below $V_{\mathrm{S}} = 4.0\,\mathrm{kms}^{-1}$ down to the Moho which is found as a sharp discontinuity at 34 km. In the uppermost mantle $V_{\mathrm{S}} = 4.7\,\mathrm{kms}^{-1}$ is found.

An abrupt Moho discontinuity is also confirmed by MZK (Fig. 5G). Semblance forms a pronounced and distinct maximum indicating the Moho at a depth of 33 km and a rather high $V_{\mathrm{P}}/V_{\mathrm{S}}$ ratio of $V_{\mathrm{P}}/V_{\mathrm{S}} = 1.84$. The discontinuity at 19 km is not resolved but increased semblance is found at depths between 15 and 20 km. In contrast we find very high semblance for shallow depths between 2 and 4 km which is consistent with the thin shallow layer found from the modelling of the $V_{\mathrm{S,app}}(T)$ curves (Fig. 5B,C).

4.3 IPM

Receiver functions at station IPM show a positive conversion close to zero time (Fig. 6A), indicating high near-surface velocities. This is indicative of imperfect seismogram rotation. Furthermore, converted phases are found at 2 s and 3.5 s corresponding to a conversion at a crustal discontinuity and at the Moho, respectively. The phases at 10 and 13.5 s may be associated to multiples, although arrivals are rather early if they correspond to the direct conversion at 3.5 s.

The V_{S}-depth models obtained from apparent incidence angles (Fig. 6B) support these observations. Upper crust velocities ($V_{\mathrm{S}} = 3.6\,\mathrm{kms}^{-1}$) seem to be separated by a discontinuity near 10 km from the lower crust where $V_{\mathrm{S}} = 4.2\,\mathrm{kms}^{-1}$. The Moho is found at 24 km depth.

Waveform inversion (Fig. 6C) confirms the $V_{\mathrm{S}} = 3.6\,\mathrm{kms}^{-1}$ but shows a thickness of about 14 km for the top layer and $V_{\mathrm{S}} = 4.1\,\mathrm{kms}^{-1}$ for the lower crust. The Moho is apparently formed by a velocity gradient between 25 to 35 km depth where V_{S} increase by $0.06\,\mathrm{kms}^{-1}$ per km. However, scattering of the models is rather high in this region. Within the upper mantle $V_{\mathrm{S}} = 4.7\,\mathrm{kms}^{-1}$ is found.

The MZK (Fig. 6G) shows increased semblance at $12 - 16$ km depth corresponding to the crustal discontinuity found before. Semblance is high within a broader depth range from 24 to 33 km. Similar to the observations from synthetic examples sensitivity to $V_{\mathrm{P}}/V_{\mathrm{S}}$ is low (compare Fig. 4) confirming the velocity gradient at Moho depth found by waveform inversion.

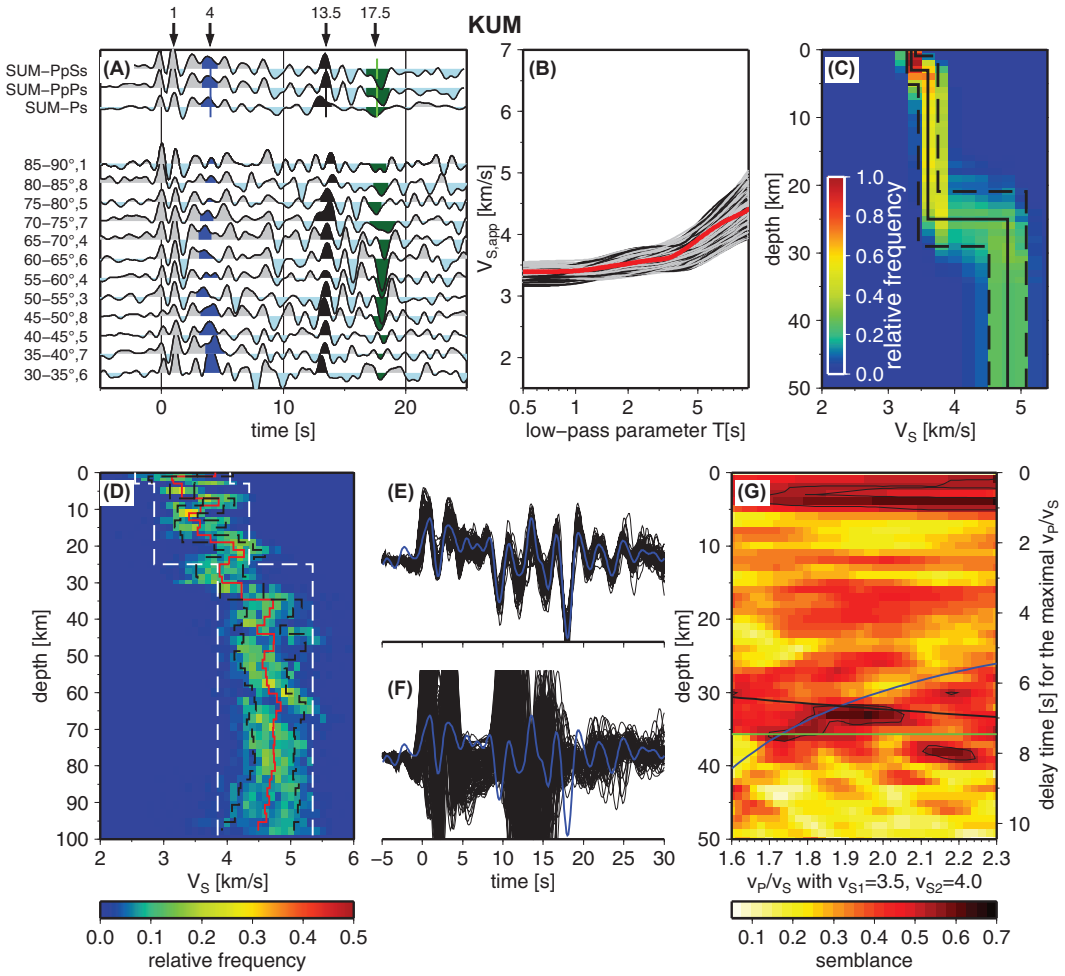

Fig. 5 Analysis of receiver functions at station KUM (see with Fig. 3 for more details). **A** Receiver functions, stacked within bins of 5° according to epicentral distance and low-pass filtered at 1 Hz. Distance ranges and number of stacked receiver functions are annotated on the left. Notice complex waveforms also for bins with larger number of observations. Arrows mark delay times of important phases. **B** $V_{\mathrm{S,app}}(T)$ curves. Grey lines: 160 mean curves ($\bar{V}_{\mathrm{S,app}}(T)$) from jackknifing. Black and red curves: synthetic $V_{\mathrm{S,app}^{syn}}(T)$ curves predicted from retrieved V_{S} models and from the medium model resulting from waveform inversion in D, respectively. **C** Density function of the V_{S}-depth models corresponding to the mean $\bar{V}_{\mathrm{S,app}}(T)$ curves in B. Black solid and dashed lines show the mean and one standard deviation. **D** red solid shows mean and black dashed lines show one standard deviation. **G** Semblance from MZK assuming 2 layers above a halfspace. Velocities of these 2 layers are $V_{S1} = 3.5\,\mathrm{kms}^{-1}$ and $V_{S2} = 4.0\,\mathrm{kms}^{-1}$. The thickness of the uppermost layer is fixed at 19 km.

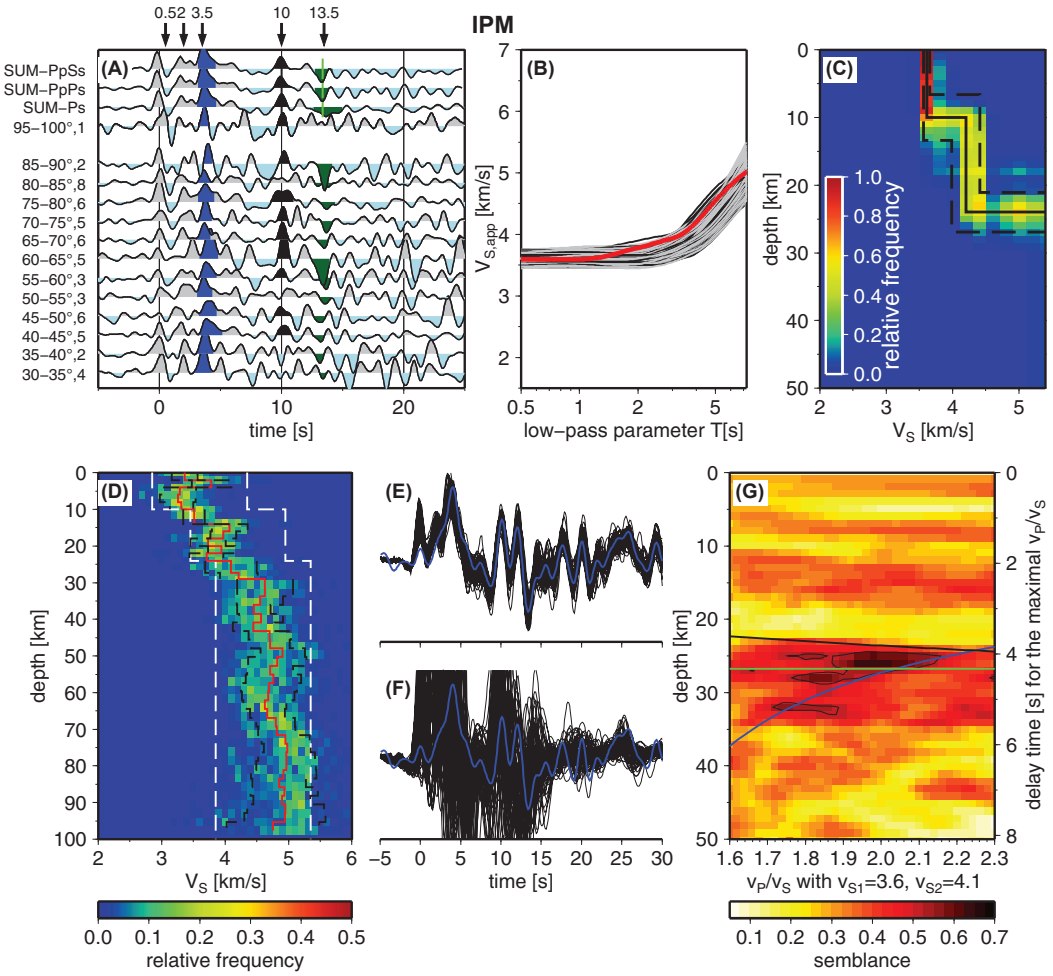

Fig. 6 Analysis of receiver functions computed from data recorded at station IPM. For MZK the thickness of the uppermost layer is fixed at 14 km. See with Figs. 3 and 5 for more details.

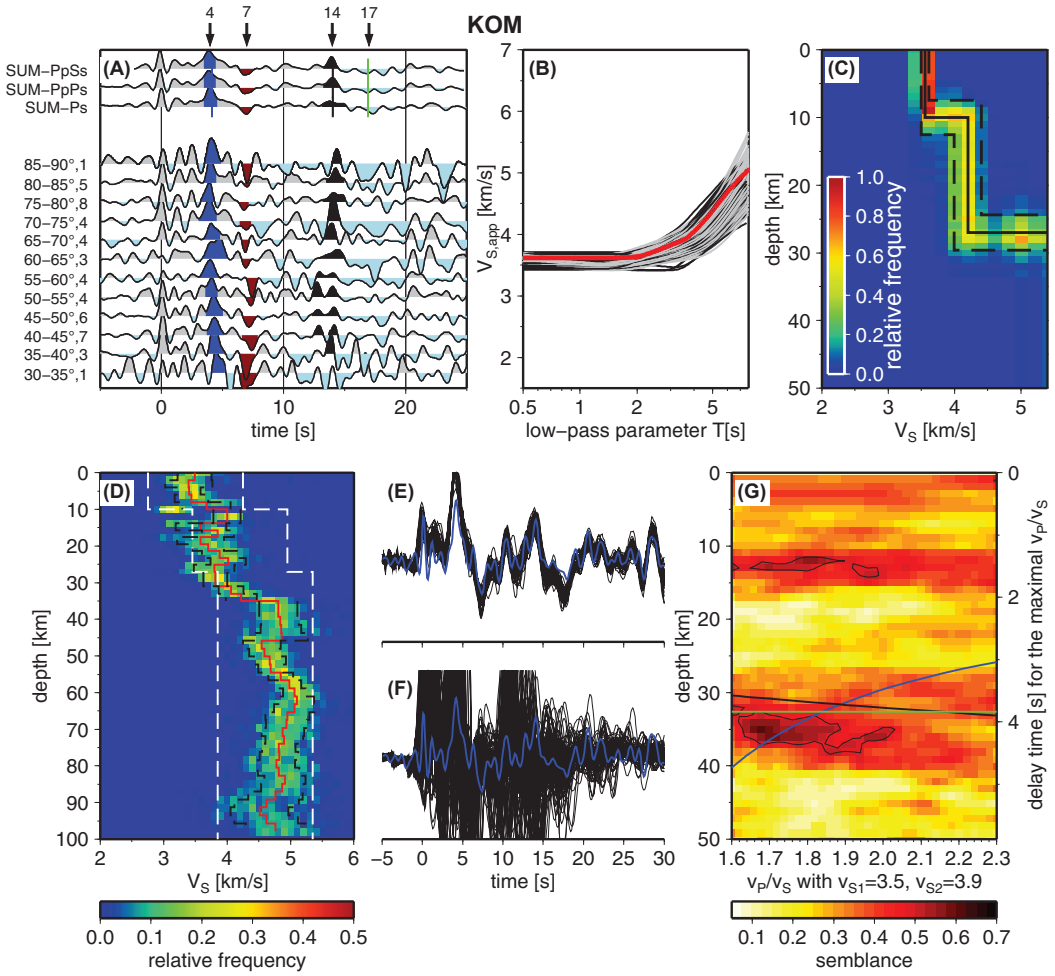

Fig. 7 Analysis of receiver functions computed at station KOM. For MZK the thickness of the uppermost layer is fixed at 12 km. See with Figs. 3 and 5 for more details.

	BSI			GSI			IPM			KOM			KUM			PSI		
	1	2	3	1	2	3	1	2	3	1	2	3	1	2	3	1	2	3
V_{S1}	**2.8**	**2.9**		**2.6**	**2.7**		**3.6**	**3.6**		**3.5**	**3.5**		**3.3**	**3.5**		**2.9**	**3.1**	
	0.1	0.3		0.2	0.3		0.1	0.3		0.1	0.4		0.1	0.4		0.1	0.5	
V_{S2}	**3.4**	**0.17***		**0.16***	**0.13***		**4.2**	**4.1**		**4.2**	**3.9**		**3.6**	**4.0**		**4.2**	**4.1**	
	0.2						0.3	0.3		0.2	0.4		0.2	0.4		0.3	0.4	
V_{S3}	**4.2**	**4.2**			**-**			**0.06***			**0.14***					**4.0**	**3.9**	
					0.03*													
	0.3	0.5														0.2	0.5	
V_{S4}	(**5.6**)	**4.8**		(**5.3**)	**4.7**		(**5.6**)	**4.7**		(**5.6**)	**4.8**		(**4.8**)	**4.7**		(**5.6**)	**4.7**	
	(0.3)	0.4		(0.3)	0.4		(0.1)	0.4		(0.2)	0.4		(0.3)	0.4		(0.3)	0.5	
H_1	**1**	**4**†		**5**	**7**		**10**	**14**	**14**†	**10**	**12**	**12**	**3**		**4**	**1**	**10**†	
	1			2			4			3		1	2		2	0		
H_2	**6**	**14**	**14**	**13**†	**15**†	**10**†								**19**		**6**	**25**	**24**
	3		3	8												4		2
H_3	(**28**)	**37**			**36**†	**31**†	(**24**)	**30**†	**26**†	(**27**)	**34**†	**35**†	(**25**)	**34**	**33**	(**33**)	**40**†	
	(4)						(3)			(3)		3	(4)		3	(3)		

Table 2 Summary of parameters (bold numbers) and their standard deviation (values underneath) retrieved by three different methods. 1=Results from modelling of the apparent incidence angle (Note that for stations BSI and PSI a fourth layer was introduced during the grid search). 2=Results from waveform inversion. 3=Results from MZK. V_S is given in [km/s], depths H in [km]. For gradients, * denote their slope [s^{-1}] and † denote their mean depth. V_{S4} denotes mantle V_S. H_3 denotes Moho depth. In brackets: values obtained from modelling of $\bar{i}_P$ which are insufficiently resolved (compare section 6).

4.4 KOM

For all epicentral distances receiver functions for station KOM show coherent signals between 0 and 10 s (Fig. 7A). A positive amplitude at 0 s indicates again imperfect seismogram rotation. The following two small positive signals probably originate from crustal discontinuities. The large positive signal near 4 s indicates a strong discontinuity in the typical depth region of the Moho. Multiples are found at 13 s (PpPs) and 17 s (PpSs). The pronounced negative signal at 7 s is probably the PpSs-multiple of the phase at $\approx$ 2 s, although it cannot be excluded that it is a direct phase from a deep structure. The PpPs-multiple of this phase interferes with the direct Moho conversion. Similar to station IPM, the model obtained from $V_{S,app}(T)$ (Fig. 7B,C) starts at high $V_S = 3.5\,\mathrm{kms}^{-1}$ for the upper 10 km followed by $V_S = 4.2\,\mathrm{kms}^{-1}$ within the lower crust. The Moho is indicated at a depth of 27 km.

Waveform inversion (Fig. 7D) confirms $V_S = 3.5\,\mathrm{kms}^{-1}$ at the surface but shows the depth of the intercrustal discontinuity slightly deeper at 12 km. The second layer with $V_S = 3.9\,\mathrm{kms}^{-1}$ is imaged down to a depth of $\approx$ 30 km. The Moho is modelled as a gradient between 30 and 35 km with a velocity increase of $0.14\,\mathrm{kms}^{-1}$ per km and an additional velocity jump at 35 km. Below, $V_S = 4.8\,\mathrm{kms}^{-1}$ indicates rather high S-wave-velocity in the mantle.

The MZK (Fig. 7G) confirms depth of the crustal discontinuity and of the Moho at $12 - 13$ km and at $33 - 40$ km, respectively. In both cases, $V_P/V_S \approx 1.8$ although resolution is low.

4.5 PSI

Receiver functions at station PSI are complex although seismograms from 75 events could be included (Fig. 8A, Tab. 1). A strong conversion from a very shallow interface indicated at 0.5 s is followed by a negative signal at $\approx$ 1 s. The positive phase at 4.5 s may correspond to the conversion at the Moho. A clear identification of its multiples is difficult. Thereafter, coherently signals appear at 9 and 10.5 s (positive) and at 12 s (negative). Either the phase at 9 s or 10 s may be indicative of the slab, as the top of the subducted plate is found at approximately 100 to 150 km.

Three layers are insufficient to model $\bar{V}_{S,app}(T)$ (Fig. 8B,C) because a minimum is observed at $T = 4$ s indicating a zone of decreased V_S. Therefore a fourth layer was introduced. The resulting density-function shows a 1 km thick layer with V_S=2.9 kms^{-1}. Then, the V_S increases at a sharp discontinuity to the high value of $V_S = 4.2\,\mathrm{kms}^{-1}$ followed by a decrease at 6 km depth to $V_S = 4.0\,\mathrm{kms}^{-1}$. The third discontinuity indicates the Moho at a depth of $\approx$ 33 km.

The V_S-depth model obtained from waveform inversion (Fig. 8D) starts at the surface with V_S=3.1 kms^{-1}. The transition to high V_S of the next layer seems also rapid. The mean velocity between 2 and 10 km depth is 4.1 kms^{-1}. Again, a velocity inversion is found between 10 and 25 km depth, where $V_S \approx 3.9\,\mathrm{kms}^{-1}$. Velocities increase again at 25 km depth to 4.2 kms^{-1} and at a depth of 40 km by 0.1 kms^{-1} per km. Mantle velocities of V_S=4.7 kms^{-1} are reached at 45 km. However, a low velocity zone is again indicated in the mantle for depth

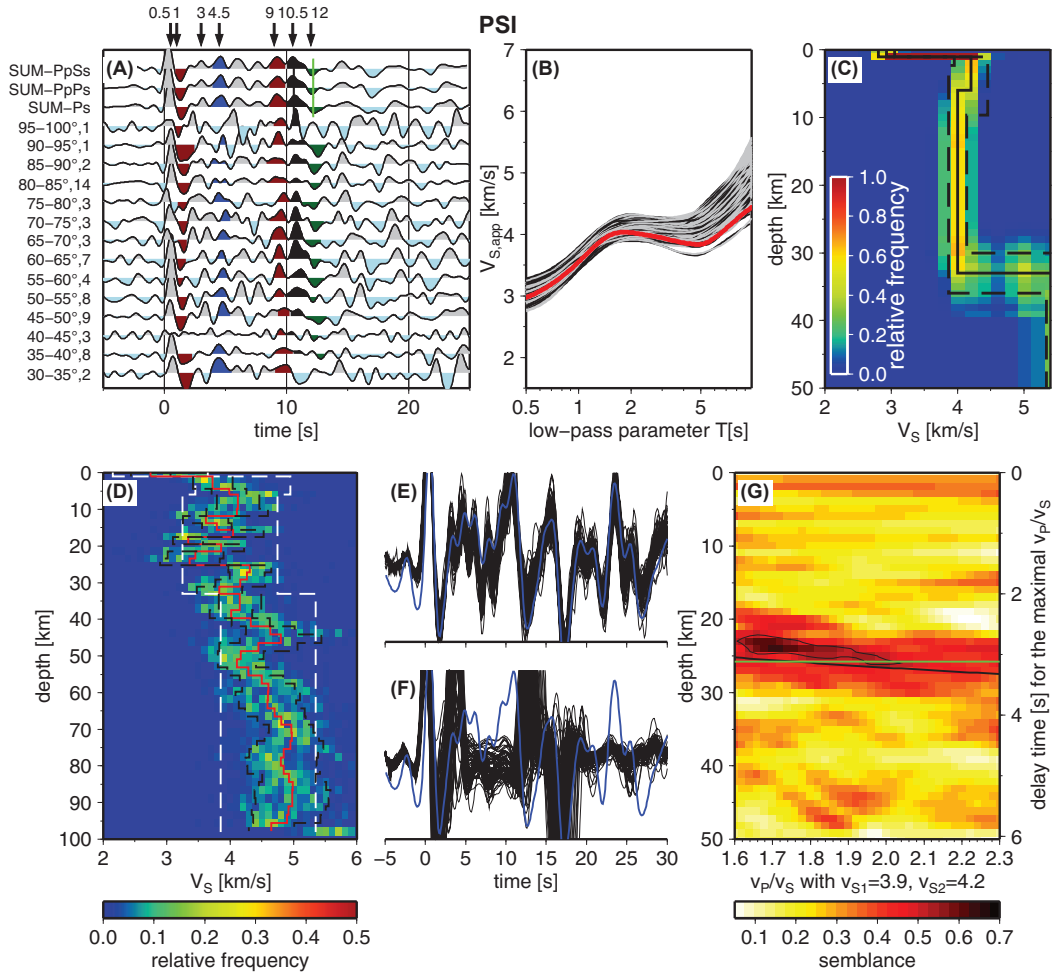

Fig. 8 Analysis of receiver functions computed from data recorded at station PSI. For MZK the thickness of the uppermost layer is fixed at 6 km. See with Figs. 3 and 5 for more details.

around 55 km. It should be noticed that standard deviations are rather high for most part of the obtained model. Therefore reliability of results from the waveform inversion is limited.

Due to the complexity of the receiver functions, the MZK algorithm is not able to resolve all of these details (Fig. 8G). Essentially, only the discontinuity observed by waveform inversion at 25 km depth is indicated in the semblance map. The more shallow discontinuity may be weakly suggested by the high semblance at 2 km depth. The velocity increase at great depth is not visible.

4.6 GSI

The receiver functions of station GSI show pronounced conversions at 2 s but also conversions with smaller amplitude at 4, 5, 6.5, and 14 s. The signal at 6.5 s could be the PpPs multiple of Ps at 2 s. The signals at 14 and 18 s could be the PpPs and PpSs multiples of Ps at 4 s.

Resulting $V_{S,app}(T)$ curves (Fig. 9B,C) reveal V_S = 2.6 kms^{-1} for the uppermost 5 km. Velocity and thickness of the second layer are not well defined but a velocity gradient seems to exist between 5 and 20 km with 0.16 kms^{-1} per km. During waveform inversion (Fig. 9D) stacking was limited to receiver functions with backazimuth between 30° and 60°, because azimuthal variations of receiver functions are observed (see section 5). It confirms the velocity of the upper layer as well as the velocity gradient that leads to V_S = 4.7 kms^{-1} at a depth of only 20 km. However, the uppermost layer appears thicker than observed from $V_{S,app}(T)$. Between 20 and 40 km depth the model shows a velocity inversion. On average V_S decreases from 4.7 kms^{-1} at 20 km V_S to only 4.3 kms^{-1} at 30 km depth. However uncertainties are rather high in this part of the model (up to 0.75 km/s). Upper mantle velocities of V_S = 4.7 kms^{-1} are reached again at 40 km depth.

The MZK shows high semblance within a broad band between 2 and 18 km depth without resolution for the V_P/V_S. This is in accordance with the velocity gradient at this depth found before. Additionally, a semblance maximum is found at 31 km depth where V_P/V_S=1.84. This corresponds to the depth of the low-velocity layer found by the waveform inversion.

4.7 BSI

At station BSI the most prominent phases are the positive signals at approximately 1, 5, and 10 s (Fig. 10A). However, their corresponding multiples are difficult to identify.

The $V_{S,app}(T)$ curves could not be sufficiently modelled with only three layers. Therefore, a fourth layer was introduced. The results (Fig. 10C) indicate a thin top layer of 1 km thickness with V_S=2.8 kms^{-1}. In the following layer V_S = 3.4 kms^{-1} down to 6 km depth. Below this we find V_S = 4.2 kms^{-1} down to a depth of 28 km.

Due to the lack of clear multiples, waveform modelling at this station is difficult (Fig. 10D). The density-function of V_S-depth models confirm the low velocity of 2.9 kms^{-1} near the surface and a rapid increase in V_S to V_S=3.9 kms^{-1} on average at a depth of 6 km. Within the following layer between 14 and 37 km depth the mean velocity is 4.1 kms^{-1}, but rather high uncertainties are observed. The mantle velocity of 4.8 kms^{-1} is reached below a discontinuity at 37 km depth. The pronounced phase at 10 s is modelled by a clear velocity increase at 95 km depth. Although this phase, which can probably be associated with a direct conversion from the slab (see next section), shows azimuthal variations, we decided to include receiver functions of all azimuths in the stack, as the slab is found in great depth and does not have influence on the results for the shallower layers.

The MZK shows regions of high semblance between 2 and 4 km and between 6 and 8 km depth confirming the increases in velocity found before. Highest semblance are attained between 12 and 17 km depth. However, this zone of high semblance is probably caused by a misinterpretation of the phase at 10 s as a multiple. We have reasonable evidence that this phase is a direct phase. This will be discussed in the next section. Here, the location of the Moho is not resolved by MZK.

5 Structures related to the subduction

Due to their proximity to the Sunda trench we pay specific attention to inclined structures possibly related to subduction at the stations BSI, PSI and GSI (Fig. 1A). There, the slab is subducted at a low angle and still rests at relatively shallow depth of less than 150 km at PSI, 100 km at BSI and less than 50 km at GSI (Gudmundsson and Sambridge, 1998). Synthetic receiver functions show that amplitudes and delay times of phases generated by conversion at inclined structures are sinusoidal and 360° periodic with backazimuth (e.g. Cassidy, 1992). On the Q-component smallest and largest amplitudes and delay times are expected in up-dip and in down-dip direction, respectively. Although delay times are equal on the Q- and on the T-component, amplitudes on the T-component vanish and reverse in up-dip and down-dip directions. In down-

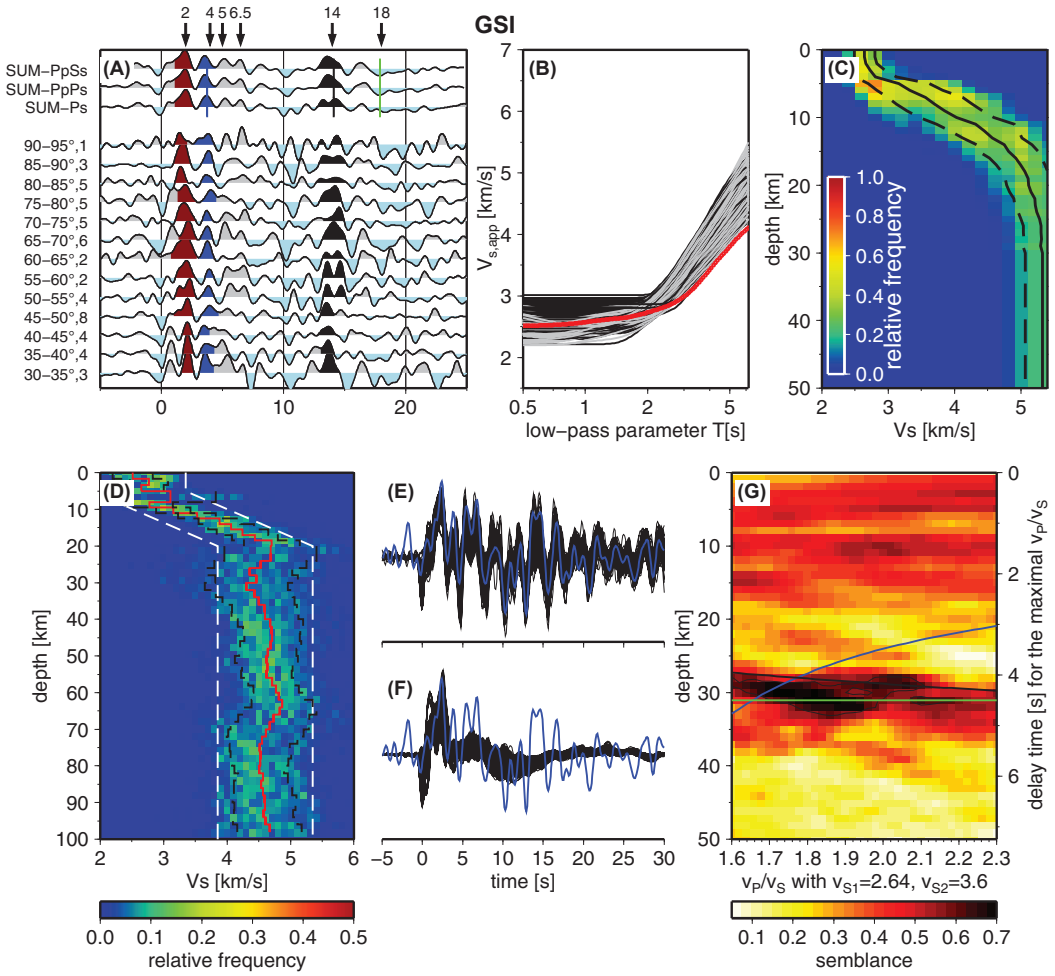

Fig. 9 Analysis of receiver functions computed from data recorded at station GSI. In D, stacking of receiver functions was limited to those with backazimuths between 30° and 60°. In C and D a clear velocity gradient above 20 km depth followed by a pronounced low-velocity zone (D) is visible. For MZK the thickness of the uppermost layer is fixed at 10 km. Notice the broad band of high semblance near 30 km supporting the observations of the velocity gradient. See with Figs. 3 and 5 for more details.

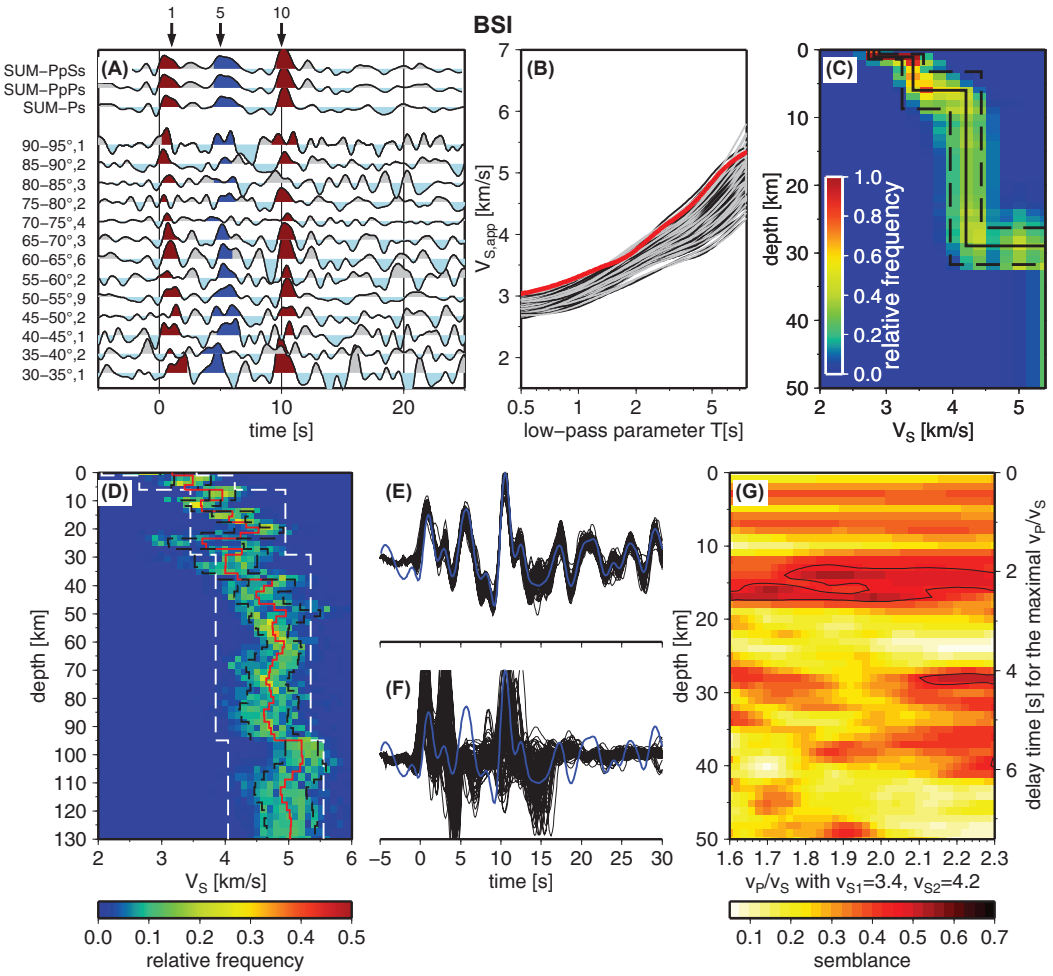

Fig. 10 Analysis of receiver functions computed from data recorded at station BSI. For MZK the thickness of the uppermost layer is fixed at 6 km. See with Figs. 3 and 5 for more details.

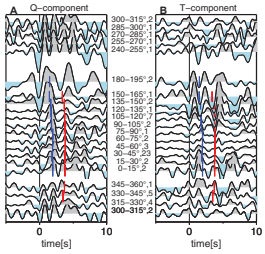

Fig. 11 Receiver functions at station GSI as a function of backazimuth. **A** Q-component, **B** T-component. Traces are corrected for moveout, low-pass filtered at 1 Hz and stacked within bins of 15° backazimuth. Blue and red ticks mark phases generated at inclined structures.

dip direction, amplitudes on the T-component change clockwise from negative to positive polarity.

Fig. 11 shows the receiver functions of station GSI as a function of backazimuth. Two important conversions in the receiver functions, possibly related to inclined structures, are highlighted. For backazimuths between 0° and 180° the first conversion is found with positive amplitude on the Q-component at ≈ 2 s (Fig. 11A). At the same time on the T-component (Fig. 11B), phases with positive amplitudes are found for north-eastern directions and negative phases are found for south-eastern directions. The transition from positive to negative amplitudes is found near 90° backazimuth indicating an inclined interface with dip in N90°E direction. This interface corresponds to the apparently gradual velocity increase between 10 and 20 km inferred from waveform inversion and can be associated to the top of the subducting slab. The depth location is in agreement with findings from reflection seismic surveys (Kopp et al, 2001). Franke et al (2008) image the top of the subducting oceanic plate at ≈ 16 km beneath the outer-arc high on which station GSI located.

On the T-components, an additional phase with a similar behaviour is found at 4 s. There, amplitudes reverse at 60° backazimuth from positive in northern direction to negative in south-east. This indicates an inclined interface dipping N60°E. On the Q-component, this phase is generally positive. Phase identification is however difficult in up-dip direction which might be attributed to the low number of observations. This phase can be associated to the second velocity increase found by waveform inversion between depths of 35 and 40 km (Fig. 9D) and may correspond inclined structures within the subducted slab.

At station BSI clear evidences for the subducting slab can be found. A pronounced positive phase was found before at 10 s (Fig. 10A). In north-east directions the delay times of this phase depend clearly on the distance of the trench to their piercing points at 100 km (Fig. 12A,B). This again indicates an inclined interface with dip to the north-east. Fig. 12C,D shows that the delay times of this phase vary strongly with backazimuth. The highest delay time is found for the $60 - 75°$ backazimuth bin. The change in polarity is found on the T-component at N60°E constraining the dip direction of the discontinuity. The negative phase at $8 - 9$ s preceding the positive phase indicates a low velocity zone related to the slab. Yuan et al (2008) and Tibi et al (2008) suggested that such a low velocity zone may correspond to the subducted oceanic crust that has not yet eclogised. The following velocity increase represents the Moho of the subducted plate. On the other hand, Peacock (1993b) states that the slab can transport large amounts of water to depths of ∼ 100 km. Released water will migrate upward into the mantle wedge causing hydration reactions or partial melting (e. g. Peacock, 1993a,Kawakatsu and Watada, 2007), causing decreased seismic velocities.

To estimate the dip of the interface, the delay times of the signal near 10 s on moveout-corrected receiver functions are converted to location of the piercing points and their shortest distances to the trench x. An upper mantle velocity of $V_P = 8.1\,\mathrm{kms}^{-1}$ and $V_P/V_S = 1.8$ is used to calculate relative depths of conversion H. Hereby it is assumed that the slab is at 100 km depth at station BSI (see Fig. 1). The dip α of the inclined interfaces is retrieved assuming the linear relation

$$H(x) = \tan(\alpha)\, x + H_0. \tag{7}$$

In (7) H_0 is the depth of the interface at the piercing point closest to the trench. The solutions and the re-

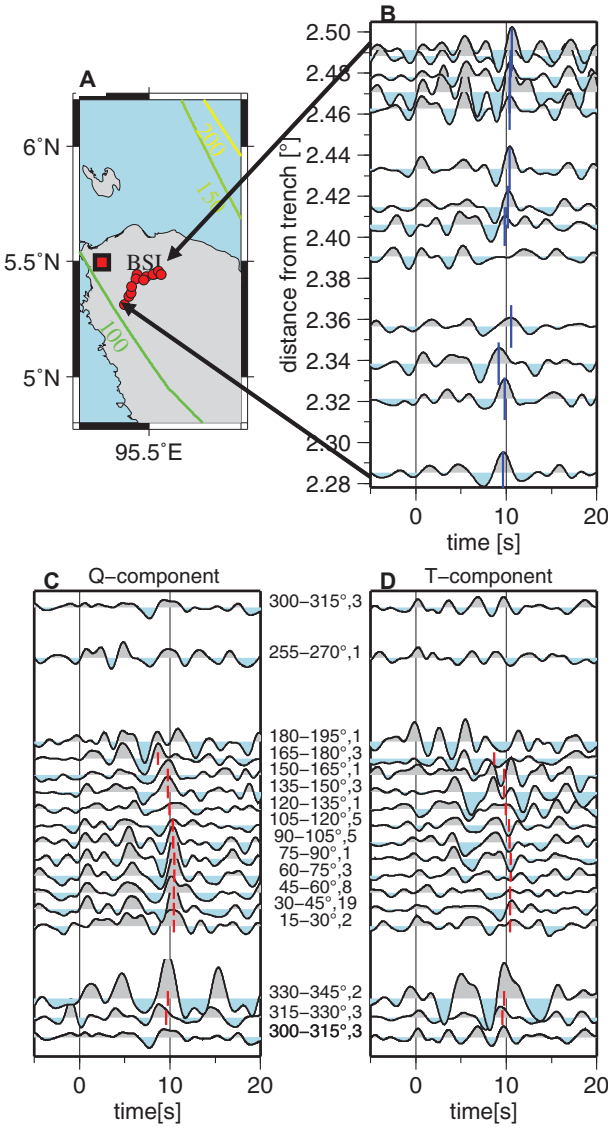

Fig. 12 Receiver functions at station BSI. **A** Piercing points (red points) corresponding to the conversions near 10 s in receiver functions (B). **B** Receiver functions as a function of distance to the trench. Traces are bandpass filtered (2 - 30 s) and corrected for moveout. Delay times of the signal near 10 s (blue ticks) increase with distance. **C, D** Q- and T-components of the receiver functions in Fig. 10 stacked within 15° wide backazimuth bins. The azimuthal dependence of arrival times of the phase near 10 s (red ticks) and polarity reversal on the T-components suggest a N60°E dipping interface.

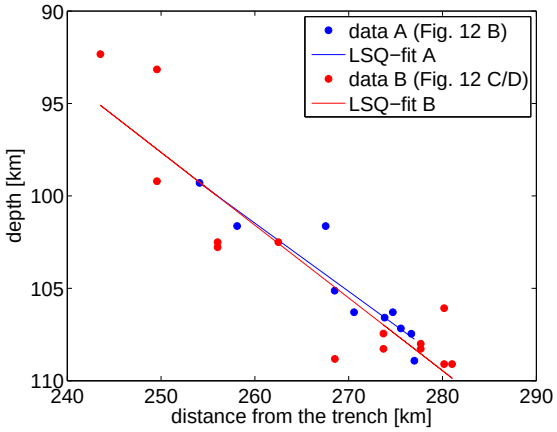

Fig. 13 Depth of conversions derived from the delay times observed at station BSI. Delay times corresponding to data A and B are marked in blue and red, respectively, in Fig. 12. For depth calculations $V_P = 8.1\,\mathrm{kms}^{-1}$ and $V_P/V_S = 1.8$ were assumed for the upper mantle. Regression lines correspond to a dip of 20° (blue, data A) or 21° (red, data B).

sulting uncertainties are found in a linear least square sense (Menke, 1989).

From the single receiver functions in Fig. 12B a dip of $\alpha = 20° \pm 9°$ at a depth of $H_0 = 99\,\mathrm{km}$ is found (see data A in Fig. 13). Using the stacked receiver functions in Fig. 12C, a similar dip angle $\alpha = 21° \pm 8°$ is obtained (see data B in Fig. 13). Assuming other P-wave velocities the variations are negligible (variations smaller than the accuracy).

From the distance of station PSI to the trench, we would expect to see a slab phase at this station as well. There are strong signals in the receiver functions at 9 s and 10.5 s which may correspond to direct phases from a structure as deep as the slab (≈ 100 km) at this station. However processing the receiver functions in a similar way as for station GSI and BSI did not reveal any evidence for inclined interfaces. This may point to a locally flat slab surface.

6 Discussion

6.1 Potential and impact of combining the methods

P-to-S converted phases show complexity of the lithosphere underneath stations located on the Sunda plate. To analyse receiver functions we combined three different methods. They include the modelling of $V_{S,app}(T)$, waveform inversion, and MZK which is a modification of the algorithm after Zhu and Kanamori (2000). Their combination results in an improved definition of V_S vs. depth. Studies of synthetic receiver functions show that V_S of the uppermost layer equals $V_{S,app}(T)$ for low T where $V_{S,app}(T)$ is constant. Depth resolution depends on data quality at long periods.

The modelling of $V_{S,app}(T)$ provides stable velocities and depth estimates for the upper layers of the model. The resolution for discontinuities deeper than 20 km decreases because $V_{S,app}(T)$ tend to diverge for high values of T due to limited data quality at long periods.

This reduces the upper limit of T for the calculation of the misfit down to 7 s at some stations. As a result the depth of the Moho is often underestimated compared to the results of the other methods used (compare Tab. 2). Additionally, there is little resolution for upper mantle velocities which requires data with high signal-to-noise at long periods. Therefore, we base the discussion of Moho depth and mantle velocities mainly on the results obtained by waveform inversion and MZK. For synthetic data, $V_{\mathrm{S,app}}(T)$ is stable even for larger T. The solutions are also affected by the parameterisation of the model in the grid search approach. The data sometimes demand up to four layers to increase the resolution in V_{S} and in depth.

The obtained V_{S}-depth models provide reference models for subsequent waveform inversions. During processing, we note that single waveform inversions are non-unique. However, a large number of inversions with different initial models results in convergence to stable final V_{S}-depth models at greater depths. They confirm the results of the $V_{\mathrm{S,app}}(T)$ modelling for shallow depths.

Retrieved shear wave velocities are used as input to MZK. For simple receiver functions, MZK provides good definitions of the depth limits of discontinuities. For sharp discontinuities also $V_{\mathrm{P}}/V_{\mathrm{S}}$ can be retrieved. However, $V_{\mathrm{P}}/V_{\mathrm{S}}$ cannot be resolved in the case of velocity gradients. This poses problems to the application of the algorithm in general, as natural discontinuities are often formed by gradients. Additionally, we find that for complex receiver functions, individual phases may be misinterpreted which leads to obscured discontinuities.

In this study receiver functions are analysed for 6 stations on the Sunda plate (compare Tab. 2). The combination of modelling of $V_{\mathrm{S,app}}(T)$ with waveform inversion provides reasonable constraints for the crustal V_{S}-depth models. The application of MZK reveals the depth of the Moho. Waveform modelling was also applied to constrain V_{S} for the upper mantle. Caused by the presence of gradient zones instead of sharp discontinuities or missing of clear multiple conversions, $V_{\mathrm{P}}/V_{\mathrm{S}}$ is generally not well resolved.

It should be emphasised, that all methods used in this study are local methods. They can be applied to single stations where dense networks are missing.

6.2 Methodological limits and approximations

The combination of the different methods balances weaknesses of the single methods and misinterpretations can be corrected. We found that modelling of $V_{\mathrm{S,app}}(T)$ needs high quality data even at long periods. Furthermore complex structures are difficult to model, as a high number of layers is needed and the results may even become non-unique. The waveform inversion turned out to be meaningless for only one single inversion. Only a statistic over a lot of trials with different initial models provides a sufficiently stable mean model. Its standard deviation serves as an estimate for uncertainties. However this method still makes some approximations which are not correct in reality. First we fixed the densities in the crust according to Birch's law. Mantle densities are fixed to $3.3\,\mathrm{g/cm^3}$. Second the $V_{\mathrm{P}}/V_{\mathrm{S}}$-ratio is fixed to 1.73 in the crust and 1.79 in the mantle. For the MZK we tried to visualise uncertainties by the 75% contour line of the semblance maximum. It turned out that plotting curves correspondent to delay times of the direct conversion and the multiples facilitates understanding of the plot.

6.3 Crust and upper mantle structures in Indonesia and Malaysia

Stations on the Malaysian peninsula (KUM, IPM, KOM) all show relatively high near-surface V_{S} of $3.3 - 3.6\,\mathrm{kms^{-1}}$ which are typical for plutonic rocks (Schön, 1996) exposed in the region (Pubellier et al, 2005). These three stations show one major intracrustal discontinuity where V_{S} increases to $4.0 - 4.2\,\mathrm{kms^{-1}}$ at depths of 12 km (KOM, ≈ 2 s arrival time), 14 km (IPM, ≈ 3 s), and 19 km (KUM, ≈ 3 s). It seems to correspond to a Conrad discontinuity separating the upper from the lower crust. The Moho discontinuity is a sharp discontinuity only at station KUM at 34 km depth, represented by a phase at ≈ 4 s. At station IPM and KOM it forms a gradient between $25 - 35$ km (≈ 3 s arrival time) and at $30 - 38$ km (≈ 4 s) depth. Obtained Moho depths are in accordance with the crustal thickness of $30 - 35$ km found by Wu et al (2005). V_{S} in the crust is on average near to the values given by Wu et al (2005). The V_{S} velocities found for the uppermost mantle in this study are higher by $0.1 - 0.3\,\mathrm{kms^{-1}}$ than the velocities given by Wu et al (2005). It should be noted however that in the surface wave tomography of Wu et al (2005) the typical resolution length is on the order of several 100 km, while it is on the order of a few 10 km for the receiver function study presented here.

The stations on Sumatra (BSI, GSI, PSI) generally indicate more complex structures. They all show significantly lower near-surface V_{S} in the range of $2.6\,\mathrm{kms^{-1}}$ at GSI and $2.9\,\mathrm{kms^{-1}}$ at PSI. At station PSI the low velocities at the surface are immediately followed by high V_{S} velocity of about $4.1\,\mathrm{kms^{-1}}$ down to 10 km depth and a complex layer with decreasing velocities

down to about 3.5 kms^{-1} in 25 km depth where velocity increases abruptly. This unusual structure may be explained by the proximity of the station to the Toba caldera. Partial melting underneath the caldera due to active volcanism (Masturyono et al, 2001) seems to result in reduction of shear wave velocities, explaining the decreasing velocities in the middle crust. The absolute value of V_S in the depth range from about 2 km to about 10 km are very high compared to normal continental upper crust making a mainly felsic composition unlikely (Christensen and Mooney, 1995). In the lower crust below 25 km depth V_S increases again to normal values of 4.2 kms^{-1}, a velocity increase which is visible in the receiver functions by a phase at 3 s. Wu et al (2005) find low crustal velocities to the Northwest of PSI more or less halfway to station BSI but average values for the region around PSI. The Moho is formed by a gradual velocity increase between 35 and 45 km depth, causing a phase at ≈ 4.5 s. This is in accordance with the deep Moho at $\approx$ 38 km found by Sakaguchi et al (2006) in the area. A low velocity zone in the mantle around 55 km depth may also be caused by partial melting in the upper mantle. At station GSI V_S is low within the upper 5 km, indicating a thick sedimentary layer. This seems reasonable since GSI is situated on the island Nias which is part of the accretionary wedge formed by marine sediments scraped-off the subducting oceanic plate. The gradual velocity increase between 10 and 20 km probably images the top of subducting oceanic plate and is represented in the receiver functions by a broad phase around 2 s. Azimuthal dependence of delay times of converted phases and polarity reversal on the T-components provide evidence for dip of the subduction to the north-east. This is in accordance with the direction of subduction at the Sunda Arc and recent observations (Kopp et al, 2001; Franke et al, 2008; Singh et al, 2008). Within the slab another north-east dipping structure is indicated. For the corresponding observed converted phases the dip is also expressed in azimuthal variation of times and their polarity reversal on the T-components (Fig. 11). In both cases an exact quantification of the dip is difficult due to interference of different phases in receiver functions. It follows a low-velocity zone near 30 km depth and a velocity increase at $35 - 40$ km depth, causing a phase at ≈ 4 s delay time. This low-velocity zone might be indicative of serpentinisation due to water intruding the oceanic plate through faults related to bending of the slab (Ranero et al, 2005; Hacker et al, 2003). The subsequent positive conversion indicates a velocity increase and the lower limit of the serpentinised zone.

At station BSI we find $V_S = 2.8$ kms^{-1} at shallow depth corresponding to sedimentary rocks (compare Crow and Barber, 2005). Below, V_S increases to 3.8 kms^{-1} at a depth of 6 km, indicating basement rocks. V_S increases to 4.1 kms^{-1} at 14 km depth. Similar to the stations on the Malaysian peninsula this corresponds to the transition to the lower crust. This observation is mainly supported by waveform inversion and MZK. The Moho is found at a depth of 37 km, which is similar to station PSI and causes a phase at the rather high delay time of ≈ 5 s in the receiver functions. Evidences for inclined structures related to subduction are also found at BSI. A discontinuity displayed by a phase around 10 s and dipping at $20° \pm 8°$ to the north-east indicates the subducting oceanic slab at $90 - 110$ km depth and confirms earlier results (Gudmundsson and Sambridge, 1998; Widiyantoro and van der Hilst, 1996).

6.4 Comparison to other island arcs

The structure beneath the stations in Malaysia shows a clear separation between upper and lower crust and overall crustal thicknesses between 30 to 35 km comparable to continental average structure. The revealed models beneath the stations in Indonesia show overall more heterogeneity, a thicker crust and high velocities in the upper and lower crust. These characteristics are typical for island arc models (Rudnick and Fountain, 1995; Christensen and Mooney, 1995). However, the crustal V_S velocities are high in comparison to other island arcs and indicate an enhanced mafic contribution to these layers (Rudnick and Fountain, 1995). However, without knowledge of V_P and density structure a detailed association with specific rock types is not possible. The crustal structures found here are quite comparable to the one observed by Azano et al (1985) for the Japanese Archipelago close to Izu Peninsular. They determined P-velocities but S-velocities are comparable if V_P/V_S-ratios of 1.73 and 1.78 are assumed for the crust and mantle, respectively. They observed $V_P \approx 6.0$ km/s (accordingly $V_S \approx 3.5$ km/s) for the upper crust and $V_P \approx 6.8$ km/s (accordingly $V_S \approx 3.9$ km/s) for the lower crust. Both values compare well to the S-velocities of $3.3-3.6$ km/s (upper crust) and $4.0-4.2$ km/s (lower crust) found for the Malaysian stations and BSI in this study. Additionally, Azano et al (1985) also observed the Conrad discontinuity at a depth of 15 to 20 km beneath Honshu and the Moho at the relatively great depth of $35 - 40$ km. Therefore, the characteristics of the crustal structure of the Japanese island arc and the Sunda arc show similarities.

7 Conclusions

Receiver functions are often stacked to increase the signal to noise ratio with respect to single traces. However, the summation may obscure and broaden waveforms mainly of multiply converted phases when a large range of epicentral distances are included. As a result converted phases generated at sharp discontinuities and at gradients may have similar behaviour.

The combination of the different methods to analyse receiver functions, i.e. the modelling of $V_{S,app}(T)$, waveform inversion and MZK, results in V_S-depth models and resolved non-uniqueness of the individual methods. We propose that V_S is initially retrieved by modelling of $V_{S,app}(T)$ and used as input to waveform inversion. The resulting V_S-depth model is delivered to our modification of the common grid search approach by Zhu and Kanamori (2000) to compute V_S/V_P.

To estimate the depth of discontinuities and V_P/V_S the common grid search approach by Zhu and Kanamori (2000) was modified (MZK). The grid search approach by Zhu and Kanamori (2000) was extended to multiple layers. Semblance analysis was applied to retrieve model parameters. Constraining V_S instead of V_P increases resolution. In case of velocity gradients semblance is high over a broad depth range and insensitive to V_P/V_S. This may help to discriminate between sharp seismic discontinuities and gradients.

We conclude that modelling $V_{S,app}$ is a useful technique to reveal local absolute S-velocities. This can be especially useful at isolated stations where no other information are available. Furthermore, we found that the MZK significantly improves the widely used algorithm of Zhu and Kanamori (2000). Therefore, future receiver function studies may benefit from the proposed modifications.

The crustal and upper mantle seismic structure of the Sunda plate is only partly constrained from previous studies. We study the shear wave structure underneath six permanent seismic broadband stations along the Sunda Arc on Nias and Sumatra and on Malaysia by means of receiver functions. The analysis of receiver functions reveals consistent local crustal and upper mantle V_S models for the different stations. High shear wave velocities near the surface for stations on Malaysia are indicative of crystalline rocks. At near-trench stations on Sumatra low near-surface V_S correspond to thick sedimentary layers.

In general stations on Malaysia reveal crustal structures comparable to other island arcs (compare Miller and Christensen, 1994), i. e. an upper crust divided from a lower crust by the Conrad discontinuity and the Moho in relative great depth between 30 and 38 km. Stations on Sumatra and Nias show more complex crustal structures. A division in upper and lower crust as for the Malaysian stations is not identified. In contrast different low velocity zones are observed. Close to the trench those may be due to serpentinisation of the subducting slab. At distances of 120 to 150 km from the trench low S-velocities may be related to partial melting of crustal material and to volcanic activity. Additionally, the Moho is found at greater depths for stations close to the trench ($35-45$ km) than for the Malaysian stations.

Receiver functions of station GSI, located closest to the trench, show evidences for north-east dipping structures formed by subduction. Here, the top of the subducting plate is found between 10 to 20 km depth. Near station BSI the subducting slab was observed. Here, a dip of $20° \pm 8°$ to the north-east at depths between 90 and 110 km was retrieved from delay times of the Ps-converted phase. We conclude that receiver functions can be used to observe the slab and even to retrieve the local inclination of the slab surface. Again, this provides a mean to infer information about the slab in regions where seismic stations are too isolated for the application of other geophysical methods such as tomography.

Acknowledgements The considered seismic stations are operated by GEOFON (GFZ German Research Centre for Geosciences), Malaysian National Seismic Network, Pacific21, and the Japan-Indonesia Seismic Network. Data were obtained from GEOFON and IRIS. We thank W. H. Geissler, V. Schlindwein and an anonymous reviewer for their comments that helped to improve the manuscript.

References

Ammon CJ (1991) The isolation of receiver function effects from teleseismic P waveforms. Bull Seismol Soc Am 81:2504–2510

Ammon CJ, Randall GE, Zandt G (1990) On the nonuniqueness of receiver function inversions. J Geophys Res 95:15,303–15,318

Azano S, Wada K, Yoshii T, Hayakawa M, Misawa Y, Moriya T, Kanazawa T, Murakami H, Suzuki F, Kubota R, Suyehiro K (1985) Crustal structure in the northern part of the Phillippine Sea plate as derived from seismic observations of Hatoyama–off Izu Peninsula explosions. J Phys Earth 33:173–189

Baroux E, Avouac JP, Bellier O, Sébrier M (1998) Slip-partitioning and fore-arc deformation at the Sunda Trench Indonesia. Terra Nova 10:139–144

Birch F (1961) The velocity of compressional waves in rocks to 10 kilobars, part 2. J Geophys Res 66(7):2199–2224

Cassidy JF (1992) Numerical experiments in broadband receiver function analysis. Bull Seismol Soc Am 82:1453–1474

Chang SJ, Baag CE, Langston CA (2004) Joint inversion of teleseismic receiver functions and surface wave dispersion using the Genetic Algorithm. Bull Seismol Soc Am 94:691–704

Christensen NI, Mooney WD (1995) Seismic velocity structure and composition of the continental crust: A global view. J Geoph Res 100(B7):9761–9788

Crow MJ, Barber AJ (2005) Map: Simplified geological map of Sumatra. vol 31, Geological Society, London, Memoirs

Franke D, Schnabel M, Ladage S, Tappin DR, Neben S, Djajadihardja YS, Müller C, Kopp H, Gaedicke C (2008) The great Sumatra-Andaman earthquakes – Imaging the boundary between the ruptures of the great 2004 and 2005 earthquakes. Earth Planet Sci Lett 269(1–2):118–130

Gill J (1981) Andesites and Plate Tectonics. Springer, New York

Gorbatov A, Domínguez J, Suárez G, Kostoglodov V, Zhao D, Gordeev E (1999) Tomographic imaging of the P-wave velocity structure beneath the Kamchatka peninsula. Geophys J Int 137(2):269–279

Gudmundsson O, Sambridge M (1998) A regionalized upper mantle (RUM) seismic model. J Geophys Res 103:7121–7136

Hacker BR, Peacock SM, Abers GA, Holloway SD (2003) Subduction factory 2. Are intermediate-depth earthquakes in subducting slabs linked to metamorphic dehydration reactions? J Geophys Res 108(B1):2003, DOI 10.1029/2001JB001129

Hamilton W (1979) Tectonics of the Indonesian Region. US Geol Surv Prof Pap 1048:345

Hoang-Trong P, Behe L (1972) Extended distances and angles of incidence of P-waves. Bull Seismol Soc Am 62(4):885–902

Jacobsen BH, Svenningsen L (2008) Enhanced uniqueness and linearity of receiver function inversion. Bull Seismol Soc Am 98(4):1756–1767, DOI 10.1785/0120070180

Julià J, Vila J, Macià R (1998) The receiver structure beneath the Ebro basin, Iberian peninsula. Bull Seismol Soc Am 88:1536–1547

Kawakatsu H, Watada S (2007) Seismic Evidence for Deep-Water Transportation in the Mantle. Science 316(5830):1468–1471, DOI 10.1126/science.1140855

Kennett B (1991) IASPEI 1991 Seismological Tables. Research School of Earth Sciences, Australian National University, Canberra

Kind R, Kosarev GL, Petersen NV (1995) Receiver functions at the stations of the German Regional Seismic Network (GRSN). Geophys J Int 121:191–202

Kopp H, Flueh ER, Klaeschen D, Bialas J, Reichert C (2001) Crustal structure of the central Sunda margin at the onset of oblique subduction. Geophys J Int 147:449–474

Kosarev G, Makeyeva LI, Vinnik LP (1987) Inversion of teleseismic P-wave particle motion for crustal structure in Fennoscandia. Phys Earth Planet Inter 47:11–24

Krueger F, Scherbaum F, Rosa J, Kind R, Zetsche F, Hoehne J (2002) Crustal and upper mantle structure in the Amazon region (Brazil) determined with broadband mobile stations. J Geophys Res 107:2265, DOI 10.1029/2001JB000598

Küpper FJ (1958) Theoretische Untersuchungen über die Mehrfachaufstellung von Geophonen. PhD thesis, Johannes-Gutenberg-Universität Mainz

Masturyono, McCaffrey R, Wark DA, Roecker SW, Ibrahim G, Sukhyar (2001) Distribution of magma beneath the Toba caldera complex, north Sumatra, Indonesia, constrained by three-dimensional P wave velocities, seismicity snd gravity data. Geochem Geophys Geosyst 2

Menke W (1989) Geophysical data analysis: discrete inverse theory. Academic Press, New York

Metcalfe I (2000) The Bentong-Raub suture zone. Journal of Asian Earth Sciences 18(6):691–712, DOI 10.1016/S1367-9120(00)00043-2

Miller DJ, Christensen NL (1994) Seismic signature and geochemistry of an island arc: A multidisciplinary study of the Kohistan accreted terrane, northern Pakistan. J Geophys Res 99(B6):11,623–11,642, DOI 10.1029/94JB00059

Neidell NS, Taner MT (1971) Semblance and other coherency measures for multichannel data. Geophys 36(3):482–497

Peacock SM (1993a) Large-scale hydration of the lithosphere above subducting slabs. Chemical Geology 108(1-4):49–59, DOI 10.1016/0009-2541(93)90317-C

Peacock SM (1993b) The importance of blueschist → eclogite dehydration reactions in subducting oceanic crust. Geological Society of America Bulletin 105(5):684–694, DOI 10.1130/0016-7606(1993)105<0684:TIOBED>2.3.CO;2

Pubellier M, Rangin C, Le Pichon X, Dotsea working group (2005) Dotsea: A synthesis of deep marine data in Southeast Asia. Mém Soc géol France 176

Ranero CR, Villasenor A, Morgan JP, Weinrebe W (2005) Relationship between bend-faulting at trenches and intermediate-depth seismicity. Geochem Geophys Geosystems 6(12)

Ritzwoller MH, Shapiro NM, Barmin MP, Levshin AL (2002) Global surface wave diffraction tomography. J Geophys Res 107:2335, DOI 10.1029/2002JB001777

Rudnick R, Fountain D (1995) Nature and composition of the continental crust: A lower crustal perspective. Reviews of Geophysics 33(3):267–309

Rüpke LH, Morgan JP, Hort M, Connolly JA (2004) Serpentine and the subduction zone water cycle. Earth Planet Sci Lett 223:17–34

Sakaguchi K, Gilbert H, Zandt G (2006) Converted wave imaging of the Toba Caldera, Indonesia. Geophysical Research Letters 33

Schön J (1996) Physical properties of rocks, Handbook of geophysical seismic exploration, vol 18. Elsevier, Oxford

Singh SC, Carton H, Tapponnier P, Hananto ND, Chauhan APS, Hartoyo D, Bayly M, Moeljopranoto S, Bunting T, Christie P, Lubis H, Martin J (2008) Seismic evidence for broken oceanic crust in the 2004 Sumatra earthquake epicentral region. Nature Geoscience 1:777–781

Subarya C, Chlieh M, Prawirodirdjo L, Avouac JP, Bock Y, andA J Meltzner KS, Natawidjaja DH, McCaffrey R (2006) Plate-boundary deformation associated with the great Sumatra-Andaman earthquake. Nature 440:46–51, DOI 10.1038/nature04522

Svenningsen L (2007) Teleseismic receiver functions – Method development and application . PhD thesis, University of Aarhus

Svenningsen L, Jacobsen BH (2007) Absolute S-velocity estimation from receiver functions. Geophys J Int 170(3):1089–1094, DOI 10.1111/j.1365-246X.2006.03505.x

Tibi R, Wiens DA, Yuan X (2008) Seismic evidence for widespread serpentinized forearc mantle along the Mariana convergence margin. Geophys Res Lett 35(13):L13,303, DOI 10.1029/2008GL034163

Widiyantoro S, van der Hilst R (1996) Structure and evolution of lithospheric slab beneath the Sunda Arc, Indonesia. Science 271(5255):1566–1570, DOI 10.1126/science.271.5255.1566

Wiechert E (1907) Über Erdbebenwellen. Teil I: Theoretisches über die Ausbreitung der Erdbebenwellen. Nachrichten von der Königlichen Gesellschaft der Wissenschaften zu Göttingen, Mathematisch-Physikalische Klasse

Wu HH, Tsai YB, Lee TY, Lo CH, Hsieh CH, Toan DV (2005) 3-d shear wave velocity structure of the crust and upper mantle in South China Sea and its surrounding regions by surface wave dispersion analysis. Marin Geophys Res 25(1-2):5–27

Yuan X, Ni J, Kind R, Sandvol E, Mechie J (1997) Lithospheric and upper mantle structure of southern Tibet from a seismological passive source experiment. J Geophys Res 102, B 12:27,491–27,500

Yuan X, Sobolev SV, Kind R, Oncken O, Bock G, Asch G, Schurr B, Graeber F, Rudloff A, Hanka W, Wylegalla K, Tibi R, Haberland C, Rietbrock A, Giese P, Wigger P, Röwer P, Zandt G, Beck S, Wallace T, Pardo M, Comte D (2008) Subduction and collision processes in the Central Andes constrained by converted seismic phases. Nature 408(6815):958–961

Zhu L, Kanamori H (2000) Moho depth variation in southern California from teleseismic receiver funtions. J Geophys Res 105:2969–2980

A MZK: delay times of converted phases in the case of two layers over a halfspace

In the case of two layers over a halfspace delay times of P-to-S-converted phases are calculated and used in the MZK. The following formulas which are an extension to Eqs. (6) apply:

$$
\begin{aligned}
t_{\mathrm{Ps}} &= (H_1 - H_2)\left(\sqrt{V_{\mathrm{S},2}^{-2} - p^2} - \sqrt{\left(\frac{V_{\mathrm{P},2}}{V_{\mathrm{S},2}}V_{\mathrm{S},2}\right)^{-2} - p^2}\right) \\
&\quad + H_1\left(\sqrt{V_{\mathrm{S},1}^{-2} - p^2} - \sqrt{\left(\frac{V_{\mathrm{P},1}}{V_{\mathrm{S},1}}V_{\mathrm{S},1}\right)^{-2} - p^2}\right) \\
t_{\mathrm{PpPs}} &= (H_1 - H_2)\left(\sqrt{V_{\mathrm{S},2}^{-2} - p^2} + \sqrt{\left(\frac{V_{\mathrm{P},2}}{V_{\mathrm{S},2}}V_{\mathrm{S},2}\right)^{-2} - p^2}\right) \\
&\quad + H_1\left(\sqrt{V_{\mathrm{S},1}^{-2} - p^2} + \sqrt{\left(\frac{V_{\mathrm{P},1}}{V_{\mathrm{S},1}}V_{\mathrm{S},1}\right)^{-2} - p^2}\right) \\
t_{\mathrm{PpSs}} &= (H_1 - H_2)\sqrt{V_{\mathrm{S},2}^{-2} - p^2} + 2H_1\sqrt{V_{\mathrm{S},1}^{-2} - p^2}.
\end{aligned}
\tag{8}
$$

Quantities $V_{\mathrm{P,i}}$, $V_{\mathrm{S,i}}$, H_i denote velocities and depth of the lower boundaries, respectively, for layer i.